

C.4

Aero-Optics Measurement System for the AEDC Aero-Optics Test Facility

**F. L. Crosswy and A. G. Havener
Calspan Corporation/AEDC Operations**

February 1991

Final Report for Period October 1986 through December 1990

Approved for public release; distribution is unlimited.

**TECHNICAL REPORTS
FILE COPY**

**PROPERTY OF U.S. AIR FORCE
AEDC TECHNICAL LIBRARY**

**ARNOLD ENGINEERING DEVELOPMENT CENTER
ARNOLD AIR FORCE BASE, TENNESSEE
AIR FORCE SYSTEMS COMMAND
UNITED STATES AIR FORCE**



NOTICES

When U. S. Government drawings, specifications, or other data are used for any purpose other than a definitely related Government procurement operation, the Government thereby incurs no responsibility nor any obligation whatsoever, and the fact that the Government may have formulated, furnished, or in any way supplied the said drawings, specifications, or other data, is not to be regarded by implication or otherwise, or in any manner licensing the holder or any other person or corporation, or conveying any rights or permission to manufacture, use, or sell any patented invention that may in any way be related thereto.

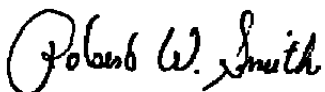
Qualified users may obtain copies of this report from the Defense Technical Information Center.

References to named commercial products in this report are not to be considered in any sense as an endorsement of the product by the United States Air Force or the Government.

This report has been reviewed by the Office of Public Affairs (PA) and is releasable to the National Technical Information Service (NTIS). At NTIS, it will be available to the general public, including foreign nations.

APPROVAL STATEMENT

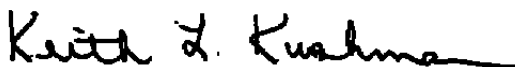
This report has been reviewed and approved.



ROBERT W. SMITH
Directorate of Technology
Deputy for Operations

Approved for publication:

FOR THE COMMANDER



KEITH L. KUSHMAN
Technical Director
Directorate of Technology
Deputy for Operations

REPORT DOCUMENTATION PAGE			<i>Form Approved</i> <i>OMB No. 0704-0188</i>	
Public reporting burden for this collection of information is estimated to average 1 hour per response, including the time for reviewing instructions, searching existing data sources, gathering and maintaining the data needed, and completing and reviewing the collection of information. Send comments regarding this burden estimate or any other aspect of this collection of information, including suggestions for reducing this burden, to Washington Headquarters Services, Directorate for Information Operations and Reports, 1215 Jefferson Davis Highway, Suite 1204, Arlington, VA 22202-4302, and to the Office of Management and Budget, Paperwork Reduction Project (0704-0188), Washington, DC 20503.				
1 AGENCY USE ONLY (Leave blank)	2 REPORT DATE February 1991	3 REPORT TYPE AND DATES COVERED Final, October 1986 -- December 1990		
4 TITLE AND SUBTITLE Aero-Optics Measurement System for the AEDC Aero-Optics Test Facility			5 FUNDING NUMBERS PE 65807F	
6 AUTHOR(S) Crosswy, F. L. and Havener, A. G., Calspan Corporation/AEDC Operations				
7 PERFORMING ORGANIZATION NAME(S) AND ADDRESS(ES) Arnold Engineering Development Center/DOT Air Force Systems Command Arnold AFB, TN 37389-5000			8. PERFORMING ORGANIZATION REPORT NUMBER AEDC-TR-90-20	
9 SPONSORING/MONITORING AGENCY NAME(S) AND ADDRESS(ES) U.S. Army Strategic Defense Command/DASD-W-WK Huntsville, AL 35807-3801			10 SPONSORING/MONITORING AGENCY REPORT NUMBER	
11 SUPPLEMENTARY NOTES Available in Defense Technical Information Center (DTIC).				
12a DISTRIBUTION/AVAILABILITY STATEMENT Approved for public release; distribution is unlimited.			12b DISTRIBUTION CODE	
13 ABSTRACT (Maximum 200 words) A fundamental problem associated with hypersonic, endoatmospheric, optically guided vehicles for interception of ballistic reentry vehicles is target image degradation caused by the complex flow field of the intercept vehicle. The image degradation mechanisms are collectively referred to as aero-optics (AO) effects. The AEDC aero-optics measurement system provides the hardware, software, techniques, and expertise for measurement of the fundamental AO effects parameters in a ground test facility. The AO measurement system is presently configured for use in AEDC Tunnel C, a continuous flow hypersonic wind tunnel. AO effects measurements are based upon image analysis, image-jitter, and holographic interferometry techniques. The primary purpose of this report is to provide hardware descriptions for the imaging and holography systems and their associated data acquisition and data reduction systems. Information is also provided in the appendixes, which describe several AO measurement technology advances in various stages of development.				
14 SUBJECT TERMS Navier-Stokes code program calibration free jet			15 NUMBER OF PAGES 87	
			16 PRICE CODE	
17 SECURITY CLASSIFICATION OF REPORT UNCLASSIFIED			18 SECURITY CLASSIFICATION OF THIS PAGE UNCLASSIFIED	
			19 SECURITY CLASSIFICATION OF ABSTRACT UNCLASSIFIED	
20 LIMITATION OF ABSTRACT SAME AS REPORT				

PREFACE

The work reported herein was performed by the Arnold Engineering Development Center (AEDC), Air Force Systems Command (AFSC), at the request of the U.S. Army Strategic Defense Command (USASDC). The USASDC Program Manager is Mr. Troy Street. Funding for this work was provided by the Strategic Defense Initiative Organization (SDIO). The work was performed by Calspan Corporation/AEDC Operations, operating contractor for the aerospace flight dynamics testing effort at AEDC, AFSC, Arnold Air Force Base, Tennessee, under AEDC Project Number DC63VL. The Air Force Project Manager is Mr. Robert Smith. This report describes work performed during the period from October 1986 through December 1989, and the manuscript was submitted for publication on February 4, 1991.

The development of and reporting for the AEDC aero-optics measurement system would not have been possible except for the close cooperative efforts of a number of management and technical specialists. Although most only worked part-time on the measurement system aspect of the overall aero-optics facility development effort, their contributions were nevertheless indispensable. In particular, the authors wish to acknowledge the following major contributors:

Calspan Program Direction	G. D. Wannenwetsch
Project Management	R. W. Cayse S. A. Stepanek
Optical and Laser System Concepts and Design	J. E. O'Hare F. L. Crosswy R. W. Menzel
Holography System Development	J. E. O'Hare A. G. Havener R. W. Payne J. H. Mansfield
Image and Interferogram Data Analysis	A. G. Havener R. W. Menzel
Data and Control System Development	T. C. Layne — Author, Section 2.2 W. E. McGregor

**Data System, Image Analysis, and
Interferogram Analysis Software**

System Software

**Optical Alignment Systems and Optical
Materials**

Code V[®] Optical Modeling

ANSYS[®] Mechanical Modeling

Mechanical Design

Laboratory and Test Operations

System Vibration Analysis

Aerodynamic Data Analysis

M. L. Askins

S. D. Kirby

L. D. Toone

**W. P. Dixon — Author,
Appendix A**

J. D. Selman

D. T. Akers

M. E. Duke

L. H. Darrell

B. C. Foust

J. H. Mansfield

W. E. McGregor

R. W. Cayse

J. P. Grubb

G. C. Cooper

CONTENTS

	<u>Page</u>
1.0 INTRODUCTION	5
1.1 Background Information	5
1.2 Aero-Optics (AO) Effects	5
1.3 Aero-Optics Imaging Parameters	6
1.4 Aero-Optics Wave Front Parameters	6
1.5 Ground Testing Support	6
1.6 Scope and Status of the AEDC AO Testing Capability	7
1.7 AEDC AO Test Facility Concept	7
1.8 AO Measurement System Development Progress	9
2.0 AERO-OPTICS MEASUREMENT SYSTEM	9
2.1 Imaging (Image-Spot and Image-Jitter) System	10
2.2 AO Data and Control System (AO-DACS)	14
2.3 Diode Laser Pulse Quality Evaluation	16
2.4 Holographic Interferometry System	16
3.0 SUMMARY AND CONCLUSIONS	19
REFERENCES	20

ILLUSTRATIONS

<u>Figure</u>	<u>Page</u>
1. Aero-Optics Effects Model	23
2. Aero-Optics Facility Concept	24
3. Transmitting and Receiving Optics for the AO Measurement System	25
4. Photographs of the Transmitting and Receiving Optics Installed in Tunnel C	26
5. Diode Laser and Control Electronics	28
6. Image Quality Evaluation	29
7. AO Data and Control System (AO-DACS)	35
8. Adjustable Time Synchronization of the Diode Laser Pulse with Respect to the Ruby Laser Pulse	36
9. Two Types of Holographic Interferometry	39
10. Holographic Reconstruction System	40

TABLE

1. Pulse Energy Statistics, 150 Pulses	41
--	----

APPENDIXES

A. Optical Performance of Heated Windows	43
B. Dynamic Laser Spot Deflector	51
C. High-Speed Image Recording Technique	53
D. Evaluation of the Integrating Sphere to Characterize Array Camera Response Nonuniformity	56
E. Initial Examinations of Subpixel Centroiding Considerations	70
F. Interferogram Analysis by Fourier Transform Interferometry	73
NOMENCLATURE	84

1.0 INTRODUCTION

1.1 BACKGROUND INFORMATION

The U. S. Army Strategic Defense Command (USASDC) is involved in developing a capability to destroy a ballistic reentry vehicle by an endoatmospheric intercept vehicle. One concept is based upon terminal optical guidance of a hypersonic intercept vehicle following ground launch and initial guidance by radar. A fundamental problem associated with endoatmospheric optical guidance at hypersonic closure rates is degradation of the target image by density effects associated with the complex flow field of the intercept vehicle. Development of a comprehensive understanding of the image degradation processes, collectively referred to as aero-optics (AO) effects, is imperative since AO effects cause errors in the target position as viewed by the interceptor.

1.2 AERO-OPTICS (AO) EFFECTS

A conceptual model used to describe AO effects has been detailed elsewhere (Refs. 1, 2, and 3); therefore, only a summary description of the AO model is presented here. An intercept vehicle in flight is represented in Fig. 1. Major features of this model include (1) a distant, hypersonic, thermally radiant target, (2) an atmospheric optical path from target to interceptor, (3) a complex hypersonic flow field in the immediate vicinity of the interceptor window, (4) an actively cooled target-viewing window in the interceptor, and (5) a target image seeker inside the interceptor. The seeker receives target radiation transmitted through the window and subsequently focuses this radiation onto a planar array of photosensors. Interceptor guidance commands are derived from photodetected, image centroid information.

AO effects are the result of index-of-refraction variations along the optical path from target to interceptor where the index variations, in turn, are related to gas density variations and, in the case of actively cooled windows, gas species effects.

Assuming distortionless performance of the window and seeker, two categories of image degradation can be identified. First, large spatial scale refractive effects caused by the interceptor bow shock, the wedge of relatively high-density air behind the bow shock as well as the wedge of coolant gas, produce a bias error in the centroid position commonly referred to as line-of-sight error or boresight error (BSE). Second, small spatial scale, turbulence-induced, refractive index fluctuations occurring primarily in the cooling gas shear layer cause a blurring of and loss of energy in the image.

1.3 AERO-OPTICS IMAGING PARAMETERS

Four parameters frequently used to describe image characteristics are BSE, Strehl ratio, image blur, and image jitter. In a ground testing environment, BSE is defined as the mean air-on image centroid position relative to the air-off reference position. Strehl ratio is the ratio of air-on peak image intensity to air-off peak image intensity. Image blur is the air-on increase in image size compared to the air-off size, and image jitter is described by the amplitude, frequency, and direction of air-on centroid position fluctuations.

1.4 AERO-OPTICS WAVE FRONT PARAMETERS

Aero-optical wave front data, used primarily to quantify aberrations induced on the optical waves, are obtainable from interferometric measurements of phase variations between sets of light waves traversing the flow field. Specific wave front characteristics attributable to path integration of optical path length changes are computed from the phase measurements. Modulation transfer function, point spread function, encircled energy, and energy zonal plots are used to quantify the wave front characteristics.

1.5 GROUND TESTING SUPPORT

In support of its efforts to develop optically guided interceptor technology, the USASDC has initiated the development of an AO ground testing capability at AEDC. The need for ground testing support stems from the fact that realization of a comprehensive understanding of fundamental AO effects represents a significant technical challenge that can more effectively and efficiently be met in a ground test environment with closely controlled flow conditions than in a flight test environment with quasi-unknown and rapidly changing conditions.

A logical progression of ground testing efforts begins with the establishment of a comprehensive and validated AO testing capability to include AO effects code development and AO effects measurement techniques to validate the codes. The establishment of credible code development and AO measurement capabilities is best carried out in a continuous flow, hypersonic wind tunnel, where the requisite extensive statistical database can be developed in a cost- and time-effective manner. Ground testing could then be extended into the domain of the blowdown and shock facilities where tunnel flow conditions more closely approach flight conditions. However, extremely short run times in these type of facilities virtually preclude development of an extensive database, and important questions arise concerning the effects upon the AO data caused by facility vibration and the transient nature of the model window heating and cooling mechanisms. In short, development of a validated AO effects prediction and measurement capability before entry into the blowdown and shock facilities may help avoid a situation where more questions are generated than are answered.

The question of AO code development and validation is important since no known arrangement of ground test facilities can simulate the entire dynamic range of Mach numbers, Reynolds numbers, gas temperatures, and flight times associated with a hypersonic interceptor. Validated codes, either ground test derived or derived from multiple flight tests will inevitably have to bridge the gap between in-flight, AO-degraded, target image data and the tracking commands to the interceptor guidance system.

1.6 SCOPE AND STATUS OF THE AEDC AO TESTING CAPABILITY

The AEDC AO testing capability is being developed for initial use in AEDC Hypersonic Tunnel C. Major elements of this capability are to include (1) an AO measurement system to measure fundamental AO parameters, (2) a probing system to measure the fundamental aerodynamic and thermodynamic flow-field parameters, (3) a proven capability to extract accurate AO data in a hostile (vibration, etc.) testing environment, and (4) AO data acquisition, data reduction, and data interpretation expertise. The all-important area of AO code development and validation is not presently included in the AEDC program.

During late FY 88, an AO system validation test was conducted in Tunnel C. Test results indicated satisfactory development progress in capability areas 1, 2, and 4, whereas unsatisfactory performance was noted for area 3. The major finding of this test was that observed AO effects were small compared to spurious system-induced effects; more details are provided in Section 1.7.

1.7 AEDC AO TEST FACILITY CONCEPT

A concept diagram for the AO Test Facility is shown in Fig. 2. The purpose of the source optics is to produce a collimated beam of laser light to simulate a distant, radiating, point source target. An image of this beam is formed by the receiving optics after the beam has interacted with the tunnel and model flow fields. In a typical testing scenario, AO measurements would be preceded by a thorough, quantitative mapping of the thermodynamic and aerodynamic flow-field characteristics using the extensive array of probing techniques available for use in Tunnel C.

The AEDC AO testing concept is based upon the premise that a diffraction-limited beam introduced into the tunnel flow field as illustrated in Fig. 2, will experience minimal AO effects between the source plate window and the model bow shock, whereas the predominant AO effects will take place between the model bow shock and the model window surface. The FY 88 test results substantiate this premise; but it was also observed that, for the ground test conditions of Tunnel C, AO effects are small, whereas spurious facility effects can be large, large enough to mask the true AO effects (Refs. 2 and 3). For example, during the

FY 88 test, BSE values in the range of tens of microradians were expected, but values in the range of hundreds of microradians were observed. This discrepancy was found to be caused by mechanical interactions of the bellows assemblies (See Fig. 2) with the source and receiving optics tables. The purpose of the bellows assemblies was to provide vibration isolation between the wind tunnel and the source and receiving optics tables while allowing evacuation of the bellows to eliminate beam distortion by convected air currents. Upon evacuation, the bellows assemblies exerted enough force on the optics tables to account for the spurious BSE effects. New bellows assemblies have been designed, which upon evacuation, exert two equal but opposite, zero-couple forces upon each optics table. This bellows redesign is expected to eliminate the large facility-induced BSE effects.

A second spurious facility effect was observed during the FY 88 test. Before installation in the wind tunnel, optical quality tests had been conducted on the AO optical system including the source plate window and the model window. The optical system produced diffraction-limited performance in the laboratory. However, once the window frame assemblies were mounted in the tunnel wall, the images were noticeably aberrated. Moreover, image quality degraded somewhat further when the windows were subjected to air-on thermal loading. Air-on differential pressure loading was avoided by equalizing the static pressure on both sides of the windows. Optical quality degradation effects caused by mechanical window stress were expected since illuminating studies in this area have previously been conducted (Ref. 1). However, the magnitude of the optical degradation effects were unexpected, especially in light of the fact that the windows were mounted in a manner that had previously and successfully been used for high-quality schlieren analysis of hypersonic flow fields. The major difference in the two applications is the 60-deg incidence angle of the AO beam at the tunnel window compared to a 0-deg incidence angle for the schlieren case. Because of the observed detrimental effect of window strain in combination with large incidence angles, an effort was initiated to develop an improved window mounting scheme since large incidence angles are a requirement for AO testing.

This effort involved modeling the mechanically induced optical effects for two window materials, fused silica and sapphire, as a function of mechanical restraint conditions plus various conditions of differential pressure and thermal loading. The entire AO optical system including window effects was then modeled and studied. At the same time, a series of laboratory experiments were conducted wherein the fused silica window and the sapphire window were subjected to the same nominal test conditions as used in the modeling study (See Appendix A for selected test results). The intent of the modeling effort was first to validate the window code by comparison of code predictions with experimental results under precisely specified and controlled laboratory conditions. Ultimately, the validated code would be used to predict the optical performance of any specified window under test facility conditions not easily simulated in the laboratory, such as the case of a large window with uniform surface

heating. The modeling effort has now progressed to the point that aberrated image size and shape predictions compare rather well with laboratory observations, although there are still discrepancies in the detailed shape of intensity contours within the boundary of the image. More importantly, though, is the fact that the window-mounting study has already resulted in the development of a much-improved, compliant frame window mounting scheme (Refs. 4 and 5).

In the compliant frame concept, a thin annulus in the window frame surrounds the window. Mechanical stress that might otherwise distort the window shape is mostly absorbed by the annulus as is mechanical stress stemming from thermal expansion of the window. The magnitude of window-induced optical aberrations for given mechanical and thermal loads are much less with the compliant frame than with a conventional frame.

With corrections now available for the two predominant facility-induced image-degradation mechanisms, the AO measurement system is ready for the second and final AO system validation test. In preparation for production testing, results of the final validation test will provide the basis for measurement uncertainty specifications for the AO parameters.

1.8 AO MEASUREMENT SYSTEM DEVELOPMENT PROGRESS

The purpose of this report is to provide detailed descriptions of the aero-optics measurement system that is being developed for the AEDC aero-optics test facility. These descriptions document the development progress to date, as well as provide some documentation needed for follow-on development of AO measurement uncertainty specifications. At the time this report was being prepared, several AO system refinements were in progress; the more important refinements are treated in Appendixes A through F.

2.0 AERO-OPTICS MEASUREMENT SYSTEM

AO effects measurements can be categorized as either wave front distortion data, as obtained by holographic interferometry, or imaging data, as obtained by image-spot and image-jitter instrumentation. A diagram of the optical system developed at AEDC to make holography, image-spot, and image-jitter measurements is shown in Fig. 3. Photographs of the optical system as installed in Tunnel C are shown in Fig. 4. The primary objective for the optical system development is, in the absence of flow-field-induced distortions, to achieve diffraction-limited performance at the focal plane defined by the planar photosensor array of the image camera. For operational efficiency and versatility reasons, secondary objectives include stipulations for an optical system that will accommodate a wide range of imaging wavelengths while allowing simultaneous operation of the holography system and the imaging system.

The primary objective has been achieved and verified as detailed in the following sections. The secondary objectives have been achieved by the use of a reflective, coaxial optics approach for the central axis of the optical system. The central axis is comprised of off-axis parabolic mirrors M5 and M10 and planar mirrors M6 to M9. Beams propagating through the central axis are collimated by M5, pass through the tunnel test section, and are then brought to focus by M10. Reflectivities of the mirror surfaces accommodate a wavelength range of 400 to 8,000 nm.

A dichroic, short-pass filter is used on the transmitting optics table to simultaneously fold the holography and imaging system light sources into the central axis beam propagation path. Standard alignment procedures (pitch and yaw adjustments of the dichroic filter, etc.) are used to implement precisely aligned, coaxial propagation paths for the collimated holography and imaging beams. This feature ensures that subsequent holographic and imaging data can be spatially correlated. In Section 2.2, an electronic scheme is described that also permits temporal correlation. After propagating through the flow field, the holography and imaging beams are separated by a dichroic, short-pass filter mounted on the receiving optics table. Mirrors M7 and M8 are supported at the ends of two hollow, structural aluminum support arms. The other ends of the support arms are firmly secured to the table tops. To reduce the detrimental effects of convection air currents, the table top ends of the support arms are sealed by flat windows, and the beam propagation paths inside the arms are evacuated.

The Code V[®] Optical Analysis System was used during development of the AO optical measurements system. For example, a Code V model of the optical system was used to predict system-induced BSE and optical aberration effects caused by small spatial orientation perturbations (pitch, yaw, roll, etc.) of each optical element about its optimum alignment orientation. The results of this study and the small AO effects observed during the FY 88 AO test indicate that even small relative motions of key AO system optical components should be measured and recorded so that an accounting can be made of their effects. At the time of this report, hardware was being assembled for this purpose. As part of this monitoring scheme, HeNe laser No. 2, XY detector No. 2, beam splitter BS2, and two planar mirrors will be used to monitor pitch and yaw motions of mirror M7 with respect to the transmitting optics table. In a similar fashion, motions of mirror M8 with respect to the receiving optics table will be monitored by HeNe laser No. 3, BS3, three planar mirrors, and XY detector No. 3. Although not indicated in Fig. 3, the HeNe laser beams transmitted through BS2 and BS3 will be used along with two XY detectors to monitor motion of the transmitting and receiving optics tables with respect to the two Tunnel C schlieren mirror mounts.

2.1 IMAGING (IMAGE-SPOT AND IMAGE-JITTER) SYSTEM

Referring to Fig. 3, the optical systems are identical, up to mirror M12, for either image-spot or image-jitter measurements. Mirror M12 is mounted on a motorized traversing stage

so that it can either be moved out of the beam path for image-spot measurements or moved into the beam path to reflect the imaging beam onto XY detector No. 1 for image-jitter measurements. With M12 moved out of the imaging beam, image-spot recordings can be acquired from the image camera at a maximum rate of 108 frames/sec. This 10^2 sample/sec rate does not even approach the 10^5 -Hz regime of turbulence-induced AO effects, and this is the reason for using XY detector No. 1 to sense high-frequency fluctuations of the image spot. The XY detector assembly developed at AEDC includes a UDT model DL10 XY displacement detector and wideband signal conditioning amplifier with a 50-ohm transmission line driving capability. The 1-db bandwidth of the XY sensor and amplifier combination is 475 kHz as determined by a dynamic laser spot deflection scheme described in Appendix B.

Optical elements with diffraction-limited specifications are used throughout the imaging system. Lenses L1 to L4 are doublets, whereas a triplet with high numerical aperture ($NA = 0.5$) is mounted inside the diode laser assembly and is used to collimate the diode laser beam. Nominal focal lengths for the imaging components are noted in Fig. 3.

The presently installed light source for the imaging system is an index-guided, GaAlAs diode laser with a rated beam power of 30 mW at a nominal wavelength of 835 nm. The diode laser assembly measures 100 mm W \times 100 mm H \times 50 mm D. This assembly consists of the diode laser mounted to a temperature-controlled heat sink, a thermistor, two miniature thermoelectric coolers, the collimating lens, a precision xyz traversing mechanism for the collimator, the control electronics for the diode laser and a preamplifier and transmission line driver for the photodiode used to monitor the output of the diode laser.

A diagram of the diode laser and its control electronics is shown in Fig. 5. Close coupling of the diode laser and its control electronics is insured by soldering the diode laser electrical leads directly to the printed circuit board for the control electronics. Emitter coupled circuitry, Q1 and Q2, with a variable current source permits rapid switching of the diode laser drive current along with a simple means for continuous variation of the drive current. Variation of the drive current along with a filter wheel with six different neutral density filters (Fig. 3) are used to set the proper irradiance level on the image camera focal plane array. The TTL to ECL level translator provides a simple way to control pulse duration and pulse repetition rate with TTL level control signals. An on-chip photodiode receives radiation from the otherwise unused rear facet of the diode laser. The photodiode signal, amplified by wideband differential amplifier IC1 and transmission line driver IC2, provides a convenient way to monitor diode laser performance. Using the circuitry of Fig. 5, laser pulse durations from 1 μ sec to continuous wave can be selected along with pulse repetition rates up to 500 kHz.

Original planning for the imaging system called for placement of the image camera at the focal plane of parabolic mirror M10. Considering the focal length of M10 and the 40- μ m

photodiode-to-photodiode spacing of the array, this camera placement would yield a nominal image centroid shift sensitivity, s , of $52 \mu\text{rad}/\text{pixel}$. However, this was considered to be too insensitive in view of expected AO effects in Tunnel C. For this reason, an angle multiplier lens L3 and imaging lens L4 were added to the optical system. An expression for the enhanced sensitivity is

$$s = \frac{K}{M} \left(\frac{1}{f_4} \right) = \frac{K}{m} \left(\frac{1}{f_{10}} \right) \frac{\text{radians}}{\text{pixel}} \quad (1)$$

where

$$M = \frac{f_{10}}{f_3} \quad (2)$$

is the angular multiplication factor

and

$$m = \frac{f_4}{f_3} \quad (3)$$

is the lateral image magnification factor, K is the center-to-center spacing for the array of photodiodes in the image camera, and f_x is the focal length of optical element x . Substituting the nominal focal length values into Eq. (1), the sensitivity of the present imaging system is calculated to be $s = 11.05 \mu\text{rad}/\text{pixel}$. This calculated value compares favorably with a sensitivity value of $s = (10.33 \pm 0.48) \mu\text{rad}/\text{pixel}$ as determined by using a precision optical wedge. The wedge was attached to a precision rotation stage and positioned between mirrors M5 and M6 (Fig. 3) so that the incident diode laser beam was approximately normal to the wedge surface. The wedge caused the beam to be deflected by an angle of $\alpha = 103.5 \mu\text{rad}$. By rotating the wedge through 360 deg , a circle of image positions was traced out on the camera photosensor array. Diametrically opposed images described a 2α sample diameter of the circle in pixel units. Dividing the 2α value by a sample diameter value produced an estimate of image sensitivity. The mean sensitivity was found to be $10.33 \mu\text{rad}/\text{pixel}$, and the standard deviation was found to be $0.48 \mu\text{rad}/\text{pixel}$.

Aside from being able to increase system sensitivity, the addition of lenses L3 and L4 leads to two other advantages. Obviously, s can easily be increased or decreased simply by changing out lens L4 for one with a different focal length. As indicated in Eq. (1), lateral magnification is also affected, but this should not cause a problem. Not so obvious is the fact that the beam between L3 and L4 is small in diameter ($\sim 2 \text{ mm}$) and nominally collimated. These two conditions are conducive to the use of an acousto-optic Bragg cell for precise and

high-speed angular deviations of the beam. As described in more detail in Appendix C, this approach, by placing multiple images on a single camera frame, shows promise for producing an effective image recording rate in the range of 10^5 images/sec. Once operational, this capability could be used to determine characteristic frequencies of turbulence-induced AO effects. Retrofit of a Bragg cell device into the imaging system is a straightforward operation.

2.1.1 Optical Quality Evaluation

As stated in Section 2.0, the primary goal in the development of the imaging system was to realize diffraction-limited optical performance. Ready availability at AEDC of up-to-date laboratory equipment and sophisticated optical system design and analysis software contributed significantly to the attainment of this goal. For example, the Zygo[®] Interferometer System was virtually indispensable for quality testing of optical components. It was particularly useful in the exacting procedure used to orient the off-axis parabolic mirrors for best performance. The imaging system, including the subtle but very important facility window effects, was painstakingly modeled and analyzed by the Code V Optical Analysis System. The ANSYS[®] physical properties software was used to model mechanical and thermal stress effects in the facility windows; this information served as input to CODE V for conversion to optical effects.

Judgments concerning the quality of images produced by the imaging system were based upon comparisons with image information generated by CODE V and by observations of sheared wave interferograms formed between optical elements M7 and M8. Optical element parameters (radii of curvature, index-of-refraction, etc.) for the imaging system, including the tunnel and model windows, were entered into the Code V analysis system and then several different situations were modeled so that the factors affecting image size could be studied. These factors include finite source size, detector geometry, and optical aberrations.

In Model No. 1, the radiation source is assumed to be a true point source, and the optical elements as well as the detector (array camera) are assumed to impart no aberrations or image distortions. The resultant diffraction-limited image is shown in Fig. 6a. The size of the image is taken to be the Airy disk diameter, the diameter that includes 84 percent of the integrated image irradiance. Using this criterion, the image size is found to be $220 \mu\text{m}$. This represents the smallest possible image for the optical system of Fig. 3 since the practical effects of source and detector geometry and optical aberrations can only lead to increased image size and distortion of the image-spot from its ideal circular shape.

An exact size specification for the radiation source emission area is not available. Consultations with the manufacturer resulted in a best estimate of $2.0 \mu\text{m}$ for the source diameter. Assuming no optical aberrations, but taking the finite source size into account resulted in the image of Fig. 6b, where an image size of $267 \mu\text{m}$ is observed. This, then,

represents diffraction-limited performance of the optical system with a finite source size of $2.0 \mu\text{m}$.

Examination of array camera effects upon image characteristics was considered important since the planar photosensor array is structured in a way that conceivably could increase the image size. Assuming a point source and taking photosensor details into account — the photodiodes are 30 by $30 \mu\text{m}$ square on $40\text{-}\mu\text{m}$ centers — yields the image of Fig. 6c where the image size is found to be $228 \mu\text{m}$. The image is seen to be only slightly affected by the photosensor array. During the course of this study, it was found that Code V could readily model source or detector geometric effects but not both at the same time. For this reason and because of the negligible effect, photosensor geometric characteristics were omitted from the optical aberration model.

Assuming a point source and modeling of optical aberration effects yielded the image of Fig. 6d. This image is virtually the same as the one in Fig. 6a. Including finite source size effects resulted in the image of Fig. 6e, which is virtually identical to the one in Fig. 6b. Since the images in Figs. 6a and b are diffraction-limited, it is clear that the Code V study predicts essentially diffraction-limited performance for the imaging system. This prediction was realized as illustrated by the actual image of Fig. 6f. The actual image-spot size of $263 \mu\text{m}$ compares rather favorably to the Code V value of $267 \mu\text{m}$, and the intensity contours are only slightly distorted compared to the ideal circular shape. The imaging optics system is now considered operational. However, a design modification to produce a diode laser source with a smaller angular size specification may be necessary so that the image size is closer to that of a true point source.

Development of the imaging optics system has been paralleled by similar levels of effort for development of the holographic interferometry system and the AO data and control system (AO-DACS). The imaging system is closely tied to the AO-DACS, which will be described next.

2.2 AO DATA AND CONTROL SYSTEM (AO-DACS)

The AO-DACS has been developed as a portable, stand-alone system that is totally independent of the testing facility main data acquisition system. This approach provides total support for AO system laboratory developments as well as test support in any testing facility. Multiple services are provided by the AO-DACS with the primary use being for imaging system control and data acquisition, archiving, reduction, and display. Secondary uses include controller functions for various motorized traversing units and data acquisition functions for various sensors such as optical alignment monitoring devices. In conjunction with a high-resolution camera, the AO-DACS will also serve as the analysis system for holographic interferometry.

During the first validation test, two separate digital machines were used to acquire, record, and reduce the image-spot and image-jitter data, and a third machine was used to reduce the holographic interferogram data. All of these functions have now been incorporated into the AO-DACS represented in Fig. 7. A DEC MicroVAX 3 supermicrocomputer serves as the host computer for the data acquisition hardware. System files and applications programs are stored by the DEC RA81 rigid disk. A DEC RA60 removable rigid disk is used for temporary data archival, and the TU81 magnetic tape drive is used for permanent data storage and system backups. Data storage for the optical alignment monitoring devices is provided by the DEC RD53 rigid disk. Graphics terminals and an LN03 laser printer are included in the system for data presentation and for data hardcopy.

Signals from the array camera, jitter sensor, and alignment monitor sensors are digitized by equipment under the direct control of the MicroVAX. A video image processor, the Recognition Concepts Inc. Model 55/256, is used for digitizing image-spot analog signals produced by the array camera. The 55/256 is also used for digitizing holographic interferograms. Digitizer modules housed in a LeCroy Model 8025 CAMAC instrument crate digitize image jitter and alignment monitor analog signals.

Another important function of the AO-DACS is to send setup commands to various pieces of equipment in preparation for a certain mode of operation. For example, the pulse width command for the diode laser is sent via the IEEE 488 bus to the HP 8112A pulse generator, which in turn, sends a programmed number of TTL-level pulses to the diode laser assembly. The output level of the diode laser is controlled by a programmed analog signal from the MicroVAX.

The "Trigger Controller" shown in Fig. 7 synchronizes the first of a set of diode laser pulses with the output pulse of the ruby laser used in the holography system. This scheme allows the holographic data to be time-referenced to a set of image-spot data or image-jitter data. An example of this capability is shown in Fig. 8 where the trigger delay was adjusted to cause the ruby laser pulse to optionally occur at the beginning, midpoint, or end of the diode laser pulse. These recorded waveforms also show the effects of a residual, potential problem: distortion of the diode laser waveform caused by electromagnetic interference (EMI) associated with the high-power pulsing circuitry of the ruby laser. Distortion of the first diode laser waveform does not, in itself, cause any problems, but it does suggest that the first image-spot of a synchronized set of image-spots could be distorted by EMI effects. At the time of this report, the EMI effects, if any, upon the first image-spot had not been determined.

2.3 DIODE LASER PULSE QUALITY EVALUATION

Measurement of low-level AO effects, as might be expected in a wind tunnel environment, calls for short-term as well as long-term stability and repeatability of the imaging system radiation source and the array camera. At the present time at AEDC, measured AO parameter statistics are derived from sets of image-spot recordings with a set containing as many as 150 individual recordings. This means that the diode laser is successively pulsed as many as 150 times during a time interval of several seconds. Ideally, the total energy delivered by each pulse should be a stable, constant value during the time period required to record a data set. Also, this value should be repeatable over a time interval as great as several hours, the time between recording of air-off tare data and air-on test data.

The short-term, pulse-to-pulse stability characteristics for the diode laser assembly presently in use at AEDC has been determined as a function of pulse-duration time. For each pulse duration, the laser power level was adjusted until 1 to 3 pixels in the image-spot were just brought to the maximum output count (255) of an 8-bit A/D converter. A total of 150 monitor photodiode waveforms were recorded, and the area (energy) under each waveform was computed. Next, the maximum, minimum, mean, and standard deviation for this set of pulse energy values were computed. The resultant data, which is included in Table 1, is normalized by the mean value.

Among the AO parameters described in Section 1.3, all but the Strehl ratio parameter are relatively insensitive to pulse energy fluctuations, but Strehl ratio errors are directly relatable to such fluctuations. Study of the Standard Deviation/Mean column in Table 1 reveals relatively stable operation except for the 750.0- μ sec pulse duration. More study of and corrections for the long pulse fluctuations are planned.

Other detailed studies to be conducted before production testing is begun include characterization of diode laser pointing stability, characterization of array camera pixel-to-pixel response uniformity, and response linearity with respect to irradiance level and the feasibility of obtaining subpixel resolution in image centroid measurements. Some preliminary information on the subjects of array camera response uniformity and subpixel centroiding are provided in Appendixes D and E.

2.4 HOLOGRAPHIC INTERFEROMETRY SYSTEM

Referring again to Fig. 3, the ruby laser radiation for the holography system is folded into the central axis of the AO measurement system by using planar mirrors M1 to M3, beam splitter BS1, and a planar, dichroic, short-pass filter. The ruby laser presently used is the 1.0 J Holobeam Model 300, but this laser is being replaced by a Lumonics Model HL52 ruby

laser with a rated output energy of 3.0 J. The beam from a 15 mW, continuous wave HeNe laser is steered by planar mirrors M1 and M2 so that it is coaxial with the ruby laser beam and is thereby used to align the optical components in the holographic system.

The two optical paths of the holographic system, the object and reference beam paths, are implemented by using 10 to 90 beam splitter BS1 to reflect 10 percent of the incident light into the object path, whereas 90 percent is transmitted into the reference path. From the beam splitter, the object waves pass through a spatial filter assembly consisting of a plano-convex, 20-mm focal length, positive lens L1, and a 100- μ m pinhole placed in the focal plane of off-axis parabola M5. The object beam waves diverge from the pinhole to overfill M5 so that the Gaussian intensity profile of the object waves flattens somewhat into a more uniform intensity distribution. A fast-response photodiode assembly is positioned alongside M5 to view a portion of the ruby laser overfill light and thereby to monitor ruby laser pulse separation times and relative pulse power levels. The output signals from the photodiode are recorded by a LeCroy Model 9400 digital oscilloscope.

As previously explained in Section 2.0, M5 is the first optical element in the central axis of the optical system, and its function is to form coaxial, collimated, diode laser, ruby laser, and HeNe laser beams. The collimated beams reflected from M5 are 3 in. in diameter and can be further reduced in diameter by a variable aperture before being projected through the test section. The object waves reflected from off-axis parabolic mirror M10 converge to a focus, pass through a short-pass filter and are directed by planer mirror M11 to the hologram recording plane, where an elliptical spot approximately 2.0 in.² in area illuminates each hologram. The spot is elliptical because the object waves intersect the hologram plane at approximately a 15-deg angle of incidence.

The reference beam originating at BS1 is directed to the hologram plate holder by using mirrors M14 to M19 with M14 to M17 serving to project the reference beam over the top of the wind tunnel. With the exception of off-axis parabolas M5 and M10, all mirrors are first surface reflectors flat to 1/20th wave and coated with the Newport ER.2 high-energy, broadband coating. In passing over the top of the tunnel, the reference beam passes through a sealed and evacuated, structural aluminum tube so that convection air currents from the hot tunnel structure will not distort the reference beam. To maintain temporal coherence, the optical path of the reference beam is made nominally equal to that of the object beam by adjusting the position of M18 to match the path length. Lenses L5 and L6 form an expanded and collimated reference beam with a 1.5-in. diam centered on the object beam spot at the hologram film plane. To achieve optimum diffraction efficiency in the holograms, the angle of incidence of the reference waves is 15 deg, which makes the outward pointing normal of the hologram surface the bisector of the angle defined by the axes of the object and reference beams. In addition to maintaining good spatial coherence, a negative lens is used for L5

to obtain noninverted ray alignment between the object and reference beams; L5 is a meniscus lens with a focal length of -31 -mm, and L6 is a positive achromat with a 335-mm focal length.

The mirror optical mount of M19 is connected to an oscillatory scanning device manufactured by General Scanning Inc. (Model MG328OT). The scanner, which allows an attached mirror to be oscillated rotationally about its vertical axis, is used to produce vertically oriented parallel fringes for the double-pulsed holographic interferograms as described in the next paragraph. The vertical fringes are an interferometric reference that is required to visualize and measure small changes in the optical phase of the object light waves. Typical mirror rotations are in the range of 10 mrad at an oscillatory frequency of 330 Hz. A development goal is to control the oscillatory amplitude and frequency so that each interferogram will have a predetermined number of reference fringes regardless of the selected time separation of the ruby laser pulses.

Figure 9 illustrates the two types of holographic interferometry being used, the first type being single-plate, double-pulse holography, and the second type being dual-plate, single-pulse holography. For the single-plate, double-pulse approach, the ruby laser emits two 25-nsec pulses separated by a short interval that is selectable from 10 to 100 μ sec. The two pulses are recorded on the same holographic plate. The reference beam is angularly shifted between the two pulses by the oscillating mirror described previously. During hologram playback, a fixed-orientation reference beam is used to reconstruct the object waves that emerge from the hologram at slightly different angles. This angular difference causes the reconstructed object waves to interfere and produce a set of vertical fringes. Since the pulse separations are short, only high-frequency disturbances (10 to 100 kHz) are capable of producing measurable changes in the interferograms. For the dual-plate, single-pulse process, individual single-pulse holograms are recorded on two separate plates. Interference is produced by precisely aligning the two holograms so that the reconstructed object waves overlap and interfere. An air-off optical reference is recorded on one plate, and an air-on test condition is recorded on the other. Since the optical waves are influenced by all of the spatial effects along the wave propagation path, the double-plate interferograms contain information that is the integrated result of the steady-state low- and high-frequency optical path differences of the air-on state referenced to the air-off state. Although these effects are inseparable in a double-plate interferogram, a theory under study is that if the amplitudes of the high-frequency phase variations are small and consistent over the optical aperture, then the variance of the spatial wave distortions determined from the double-pulse holograms might be treated as a bias that can be subtracted from the dual-plate measurements, thereby yielding phase measurements for the steady-state and low-frequency effects (Ref. 3).

Holograms are recorded on AGFA type 10E75, 4- by 5-in. glass film plates. To accommodate the emulsion-to-emulsion alignment for the dual-plate technique, the reference plate is positioned backwards in the film plate holder (the emulsion faces away from the incident ruby laser light), and the holder is translated 1.5 mm, the nominal thickness of the spectroscopic plate, toward the light source. In this way, the emulsion occupies the correct spatial position relative to the test plate during the recording step, which in turn, is the proper position for the emulsion-to-emulsion alignment to be valid during the playback step.

Holographic reconstruction is accomplished with the system represented in Fig. 10. The reconstruction beam illuminating the holograms is a 2.0-in.-diam collimated HeNe laser beam that nearly duplicates the reference beam of the holographic recording system. A television camera looks at the reconstructed object waves and furnishes an output video signal to an image processor. The image processor furnishes an output signal for visual monitoring of the interferograms as well as a digitized output for disk storage and subsequent analysis.

As discussed in Ref. 3, fringe tracking data reduction schemes and the use of Zernike polynomials is unacceptable for reducing AO-effect interferogram data. Therefore, a new method for optical phase analysis, the Fourier transform interferometry method, is being developed. The status of this new development is described in Appendix F.

3.0 SUMMARY AND CONCLUSIONS

An AO effects measurement system has been developed and successfully applied during the first of two validation tests planned for the AEDC AO test facility that is being developed for initial use in AEDC Hypersonic Tunnel C. The purpose of the first validation test was to identify system deficiencies. Two such deficiencies, one involving a bellows-type vibration isolation mechanism, and the other a tunnel window mounting scheme, were identified and corrective actions have been taken. The first objective of the second validation test is to verify that the two deficiencies have been resolved. Successful attainment of this first objective will be followed by a test matrix to provide the extensive statistical database needed to establish a credible set of measurement uncertainty specifications for the AO parameters. Development and validation of AO effects codes are viewed as major objectives during subsequent production testing.

The continuous flow and closely controlled operating conditions of Tunnel C along with its extensive array of existing flow diagnostic devices are needed for development and validation of the AO codes as well as for systematic development, refinement, and validation of the AO measurement techniques. Measurement and AO code development expertise developed in Tunnel C could be extended and applied in blowdown or shock facilities where flow conditions more closely approach flight conditions but where characteristically short test

periods preclude efficient acquisition of the number of data points needed for statistical confidence in the test results. Under these conditions, correlation of code and test data would lead to a reduction of the number of test runs needed to establish measurement and data credibility and accuracy.

The AO Measurement System provides two complementary techniques for measuring the fundamental properties of laser beam interactions with a gaseous flow field. Holographic interferometry is used for fundamental measurements of wave front distortion, whereas the imaging technique measures the centroid position shifts, blur-spot size and jitter frequencies of the image of a simulated, distant, thermally radiating target. The AO Measurement System design permits spatial and temporal coincidence of the holographic and imaging measurements. The design also accommodates the range of radiation wavelengths from 400 to 8,000 nm and exhibits diffraction-limited optical system performance.

Optical performance of the AO Measurement System exclusive of the tunnel window was considered satisfactory during the first validation test. However, several improvements will be incorporated before the final validation test is conducted. For example, the efficiency of the data acquisition, reduction, and display functions for imaging and image-jitter measurements, and the data reduction function for holographic measurements will be enhanced by incorporating these functions into a single digital data and control system instead of the present scheme involving several different digital machines. An image-jitter sensor with a 475-kHz bandwidth will be substituted for the presently used device rated at 20-kHz bandwidth. A sensor scheme for monitoring the relative motion of key optical components is also planned for implementation.

A review of array camera characteristics (photosensor geometry, responsivity uniformity, etc.) versus centroiding accuracy is needed before the final validation test. Also, the requirements for placing multiple images on a single frame of imaging data should be firmed up since multiple-image framing techniques using acousto-optic cell or scanning mirror techniques appear to be feasible.

Adaptation of the phase-demodulation scheme such as Fourier transform interferometry for analysis of holographic interferograms is advised since laboratory applications to date clearly show an advantage over the fringe-tracking/Zernicke polynomial approach. The relative advantages of phase-demodulation lie in the ability to accurately extract optical phase information in the presence of interfering background noise.

REFERENCES

1. Reiman, T. W. et. al. "Window Cooling Technology Development Program." Teledyne Brown Technical Report Prepared for the U. S. Army Strategic Defense Command Under Contract No. DASG60-85-C-0069, February 1988.

2. Cayse, R. W. et al. "Validation Tests of a Wind-Tunnel-Based Aero-Optics Measurement System at Hypersonic and Quiescent Conditions." AEDC-TSR-88-V59 (AD-B132386), April 1989.
3. Havener, A. G. and Menzel, R. W. "A Presentation of Aero-Optical Measurements in Hypersonic High Reynolds Air Flows." *Third DoD Symposium on Electromagnetic Windows*, Redstone Arsenal, AL, November 14-16, 1989.
4. Dixon, W. P. "Athermal Window Materials." *Proceedings of the Nineteenth Symposium on Electromagnetic Windows*, Georgia Institute of Technology, September 7-9, 1988.
5. Dixon, W. P. "Windows for Aero-Optical Applications." *Third DoD Symposium on Electromagnetic Windows*, Redstone Arsenal, AL, November 14-16, 1989.

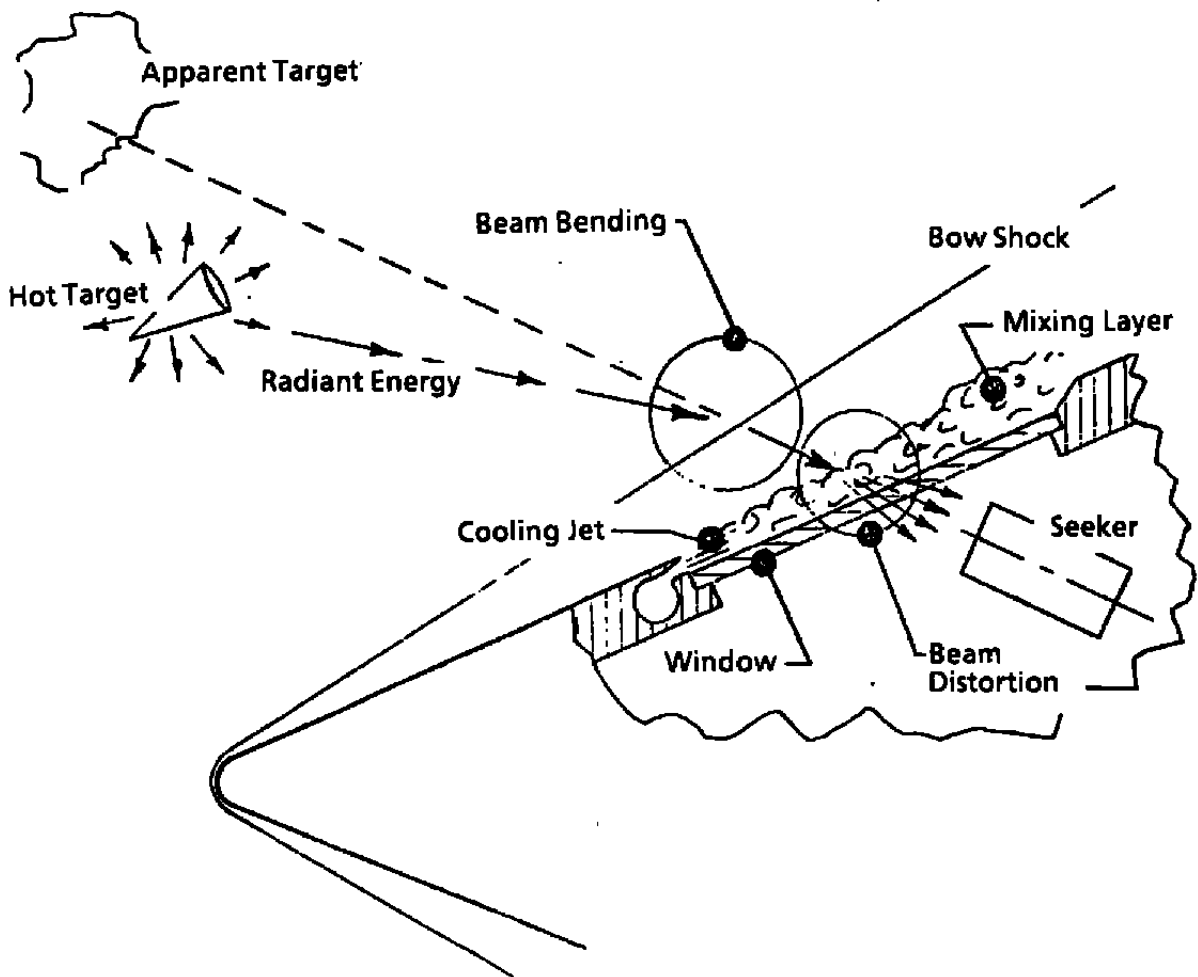


Figure 1. Aero-optics effects model.

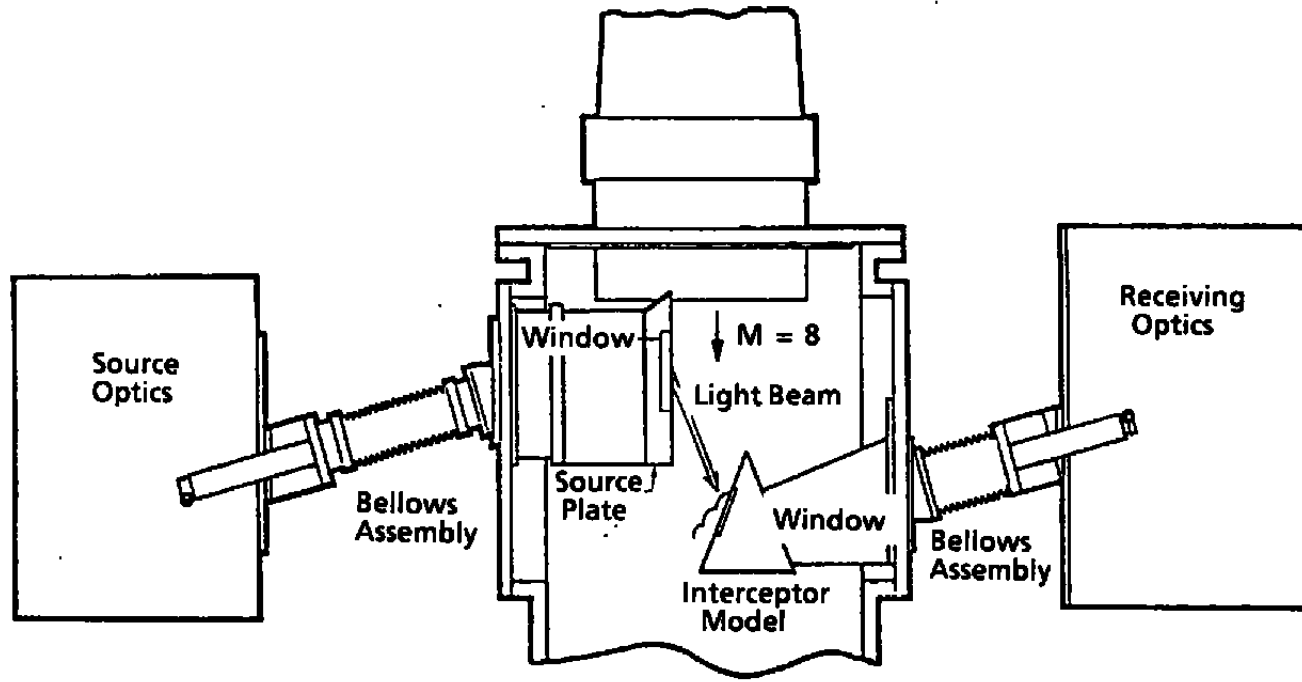


Figure 2. Aero-optics facility concept.

Optical Element Focal Length, mm

Diode Laser Collimator	8.0
L2	80.0
M5	915.0
M10	762.0
L3	40.0
L4	190.0

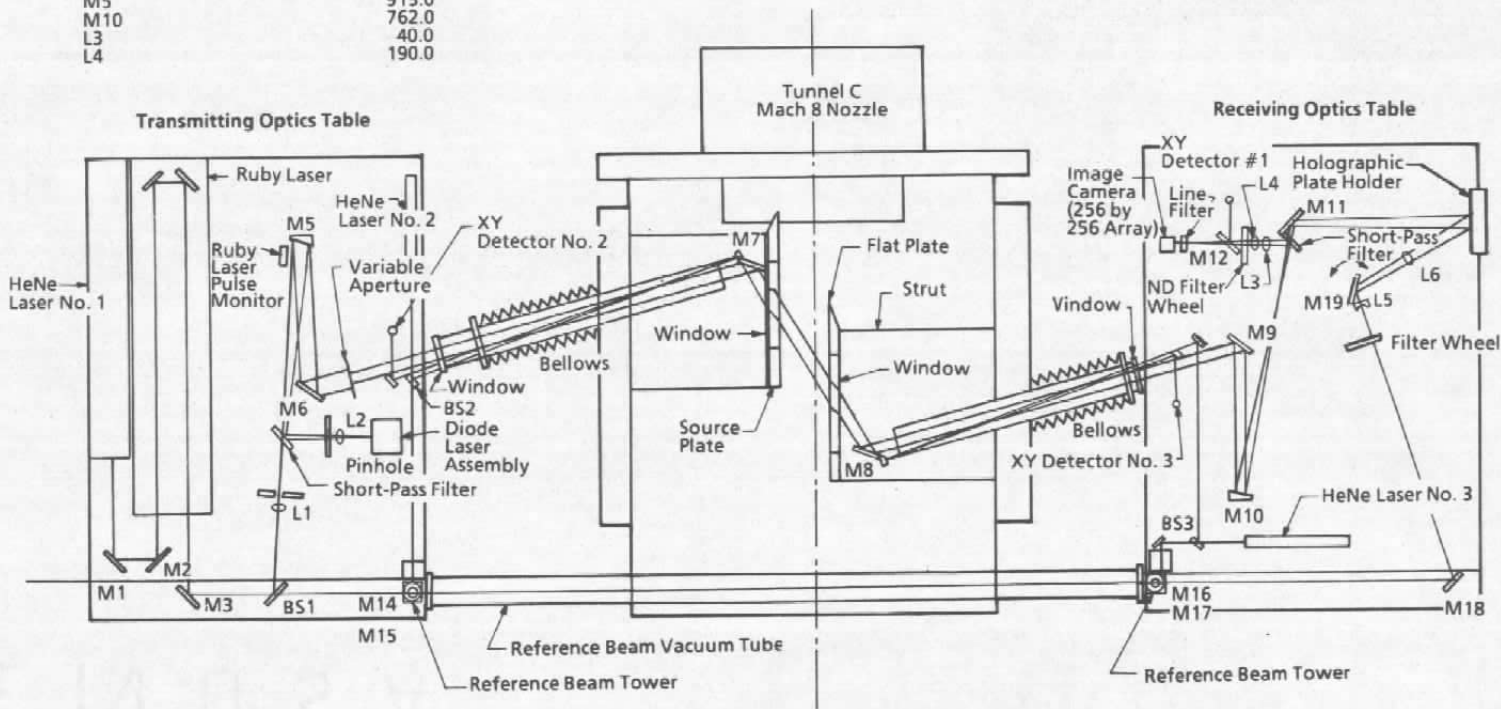
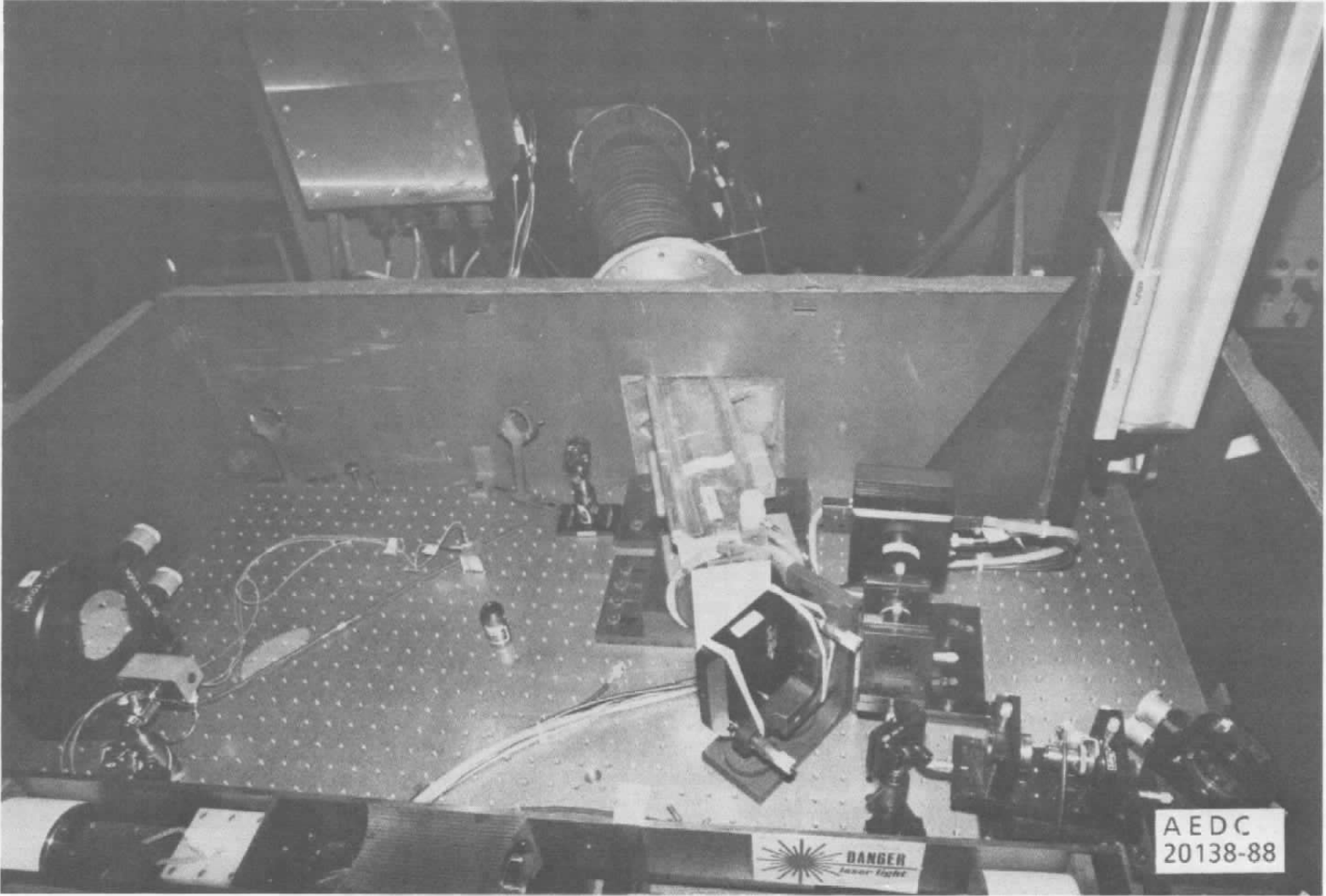
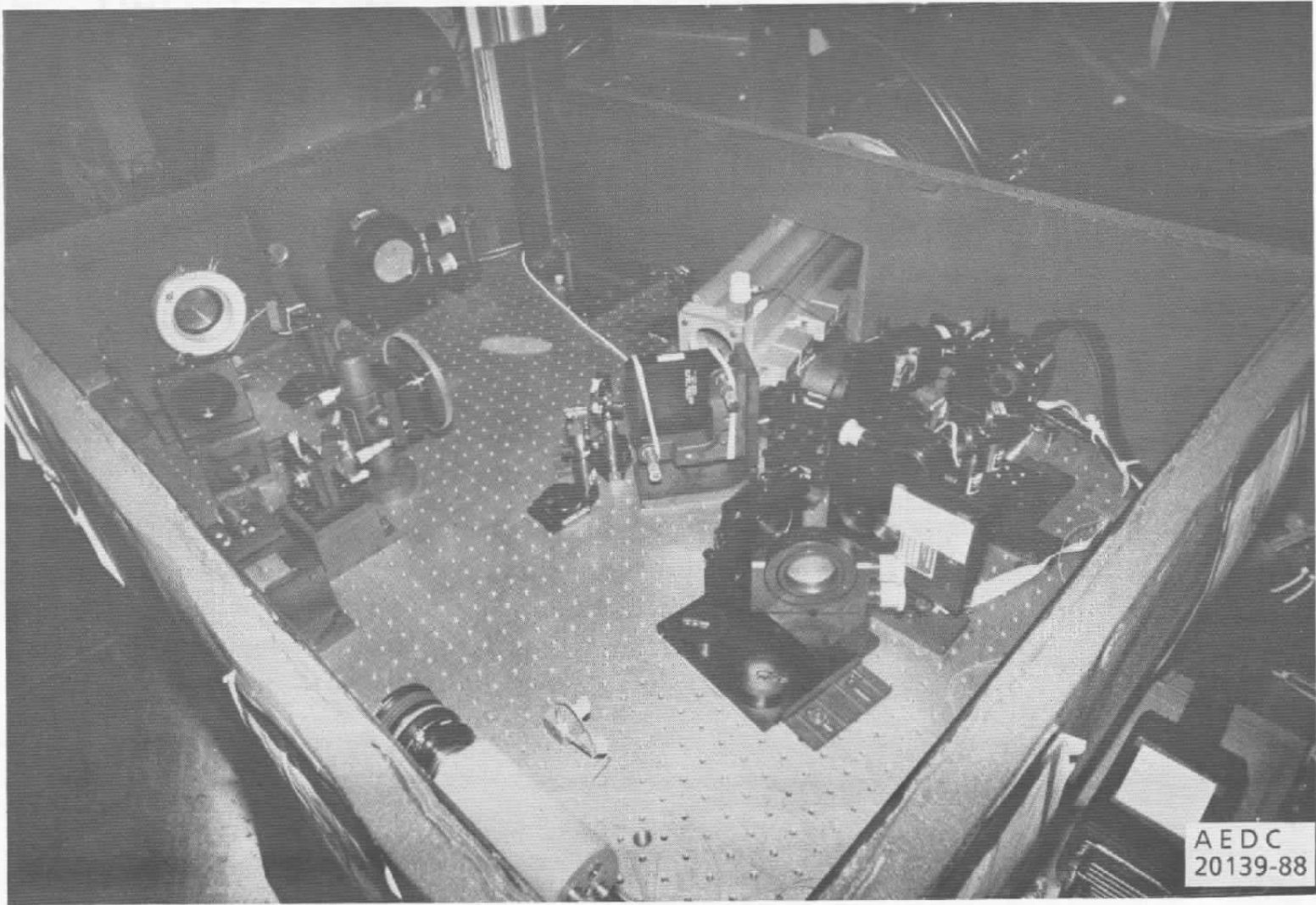


Figure 3. Transmitting and receiving optics for the AO measurement system.



a. Transmitting optics

Figure 4. Photographs of the transmitting and receiving optics installed in Tunnel C.



**b. Receiving optics
Figure 4. Concluded.**

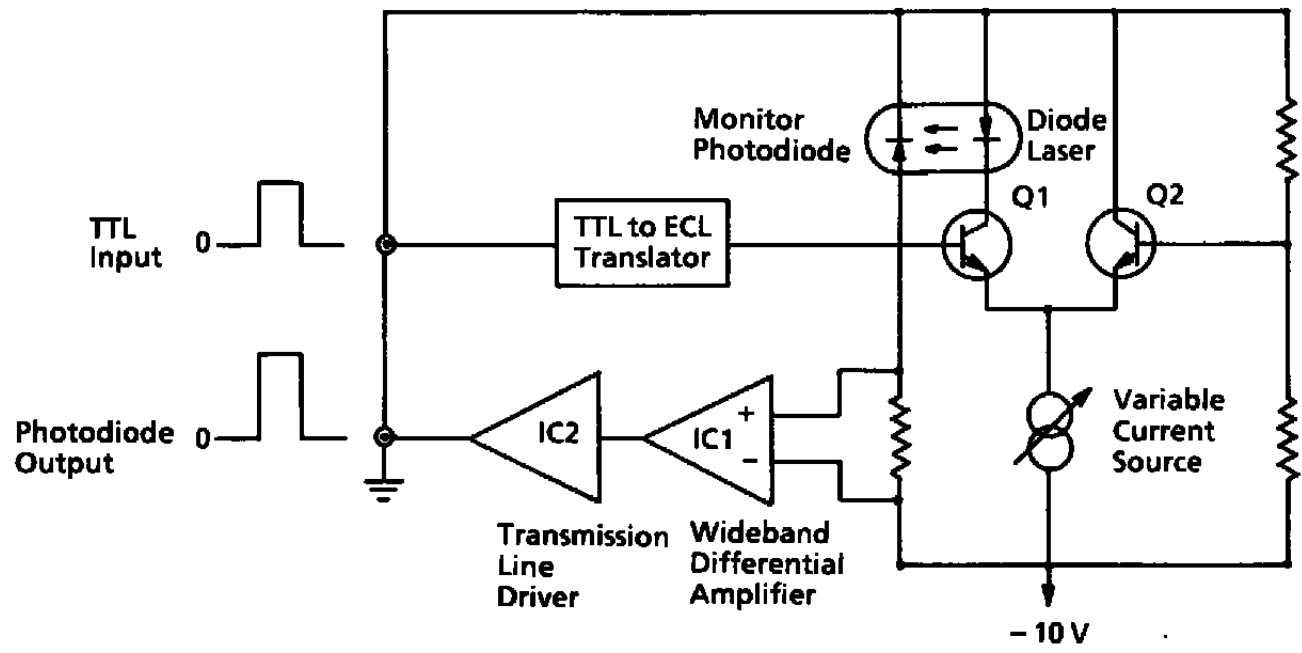
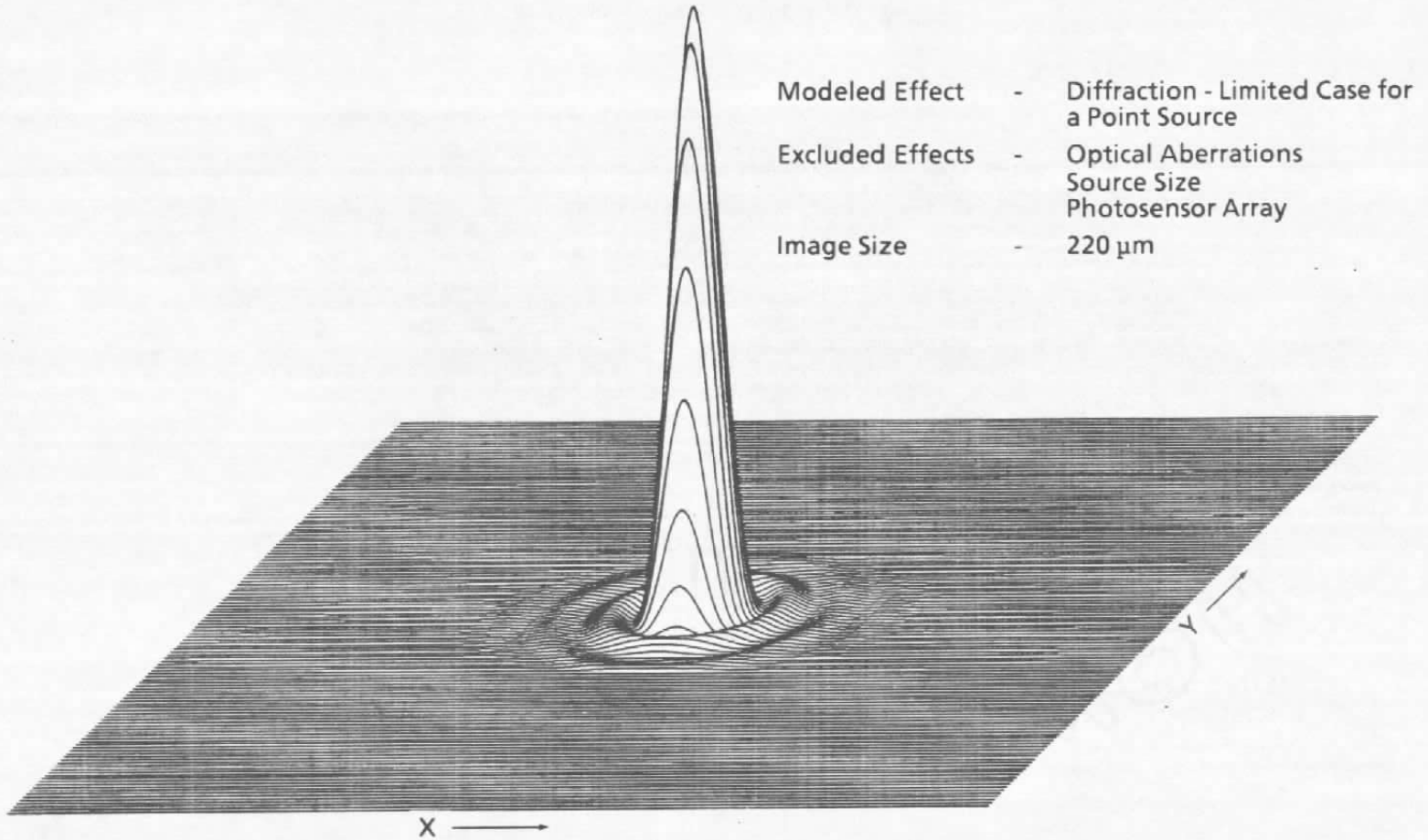
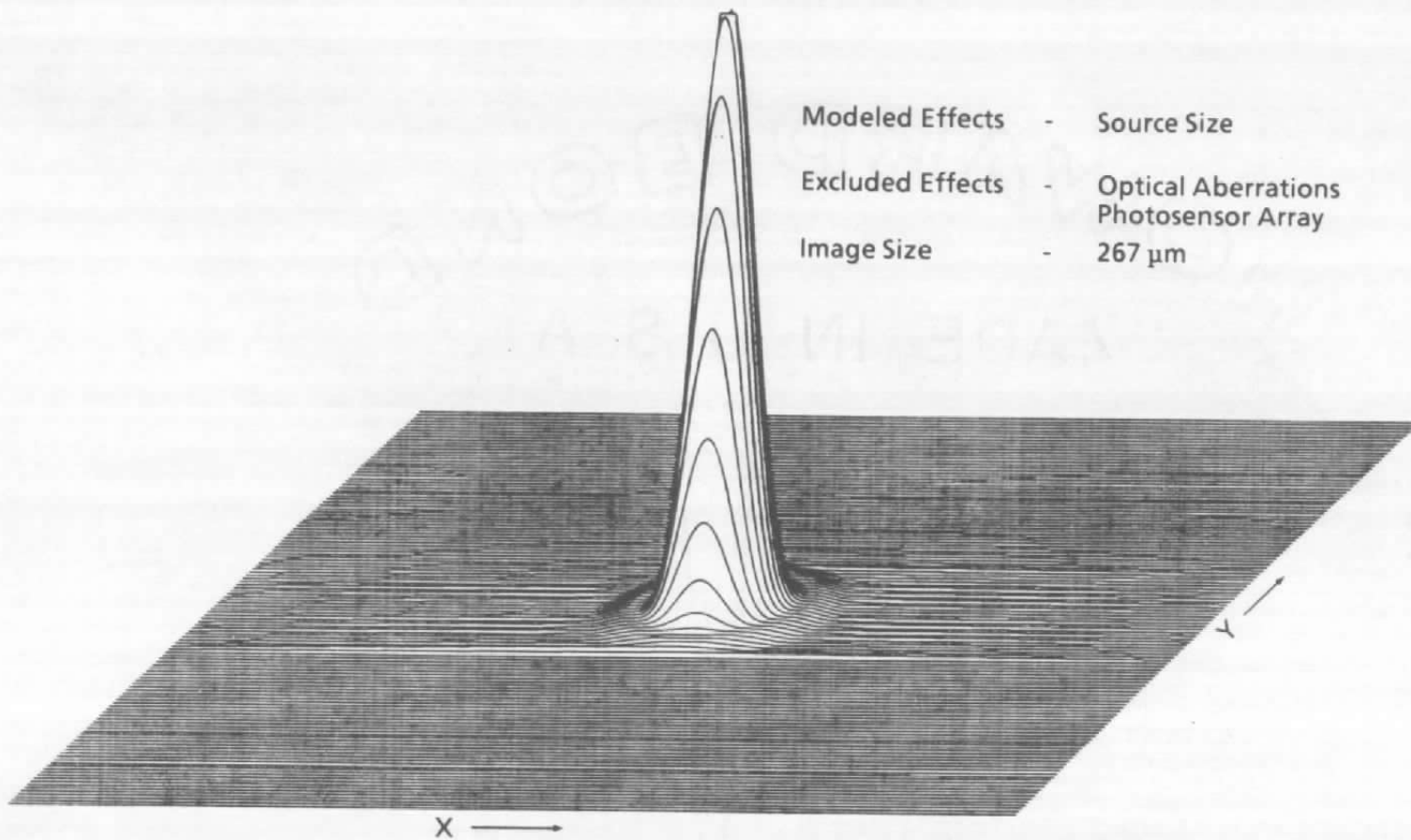


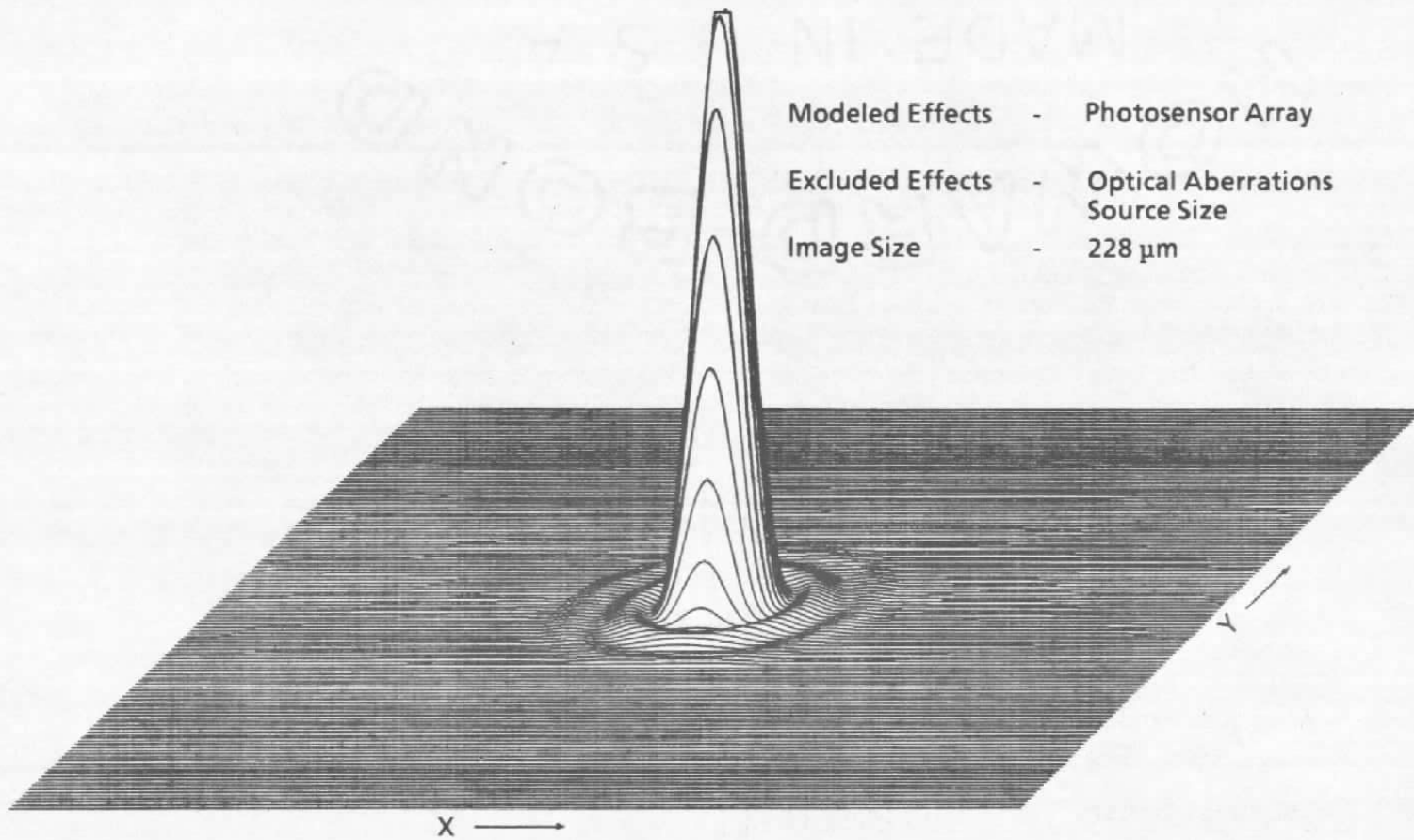
Figure 5. Diode laser and control electronics.



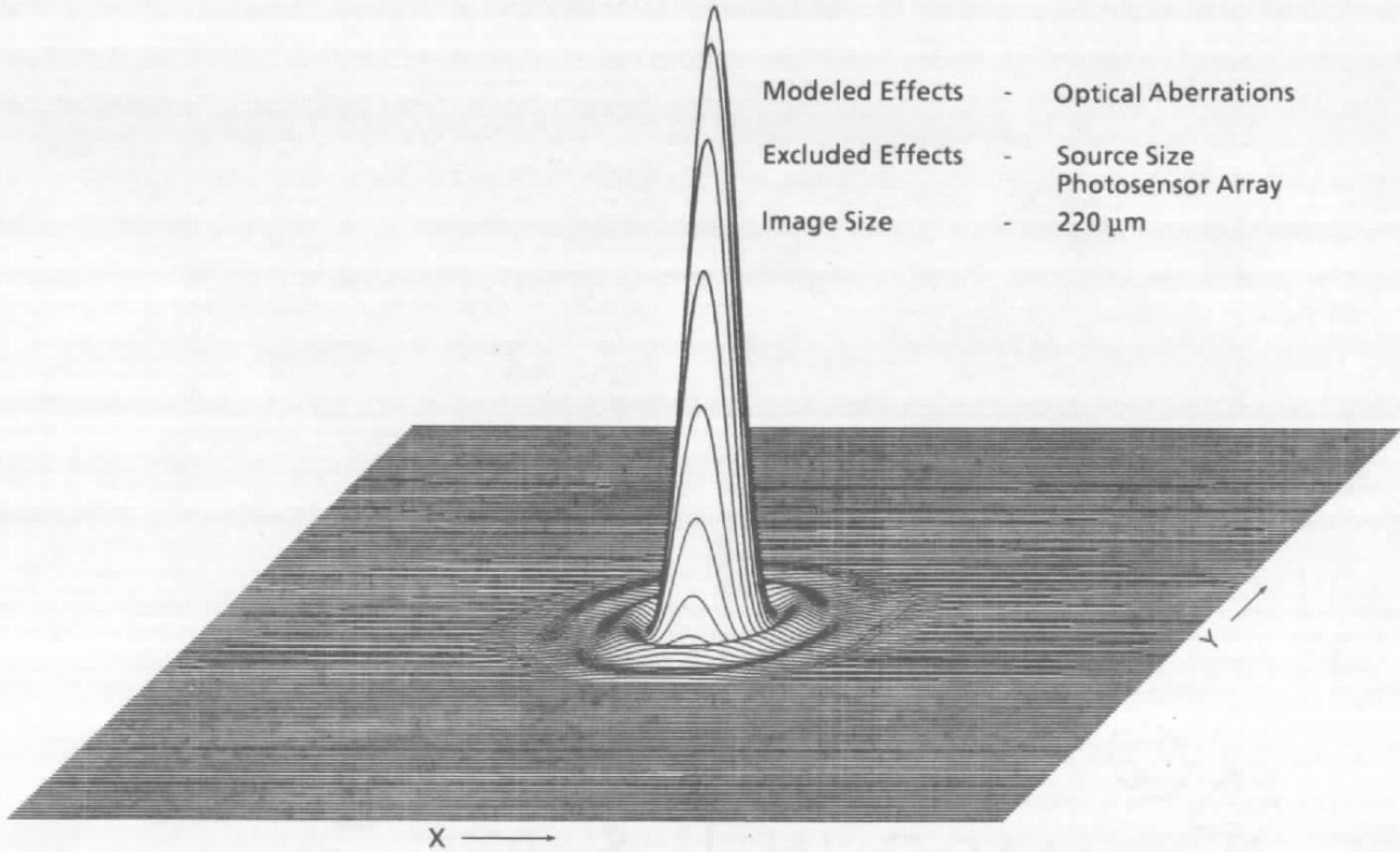
a. Code V[®] image, Model No. 1
Figure 6. Image quality evaluation.



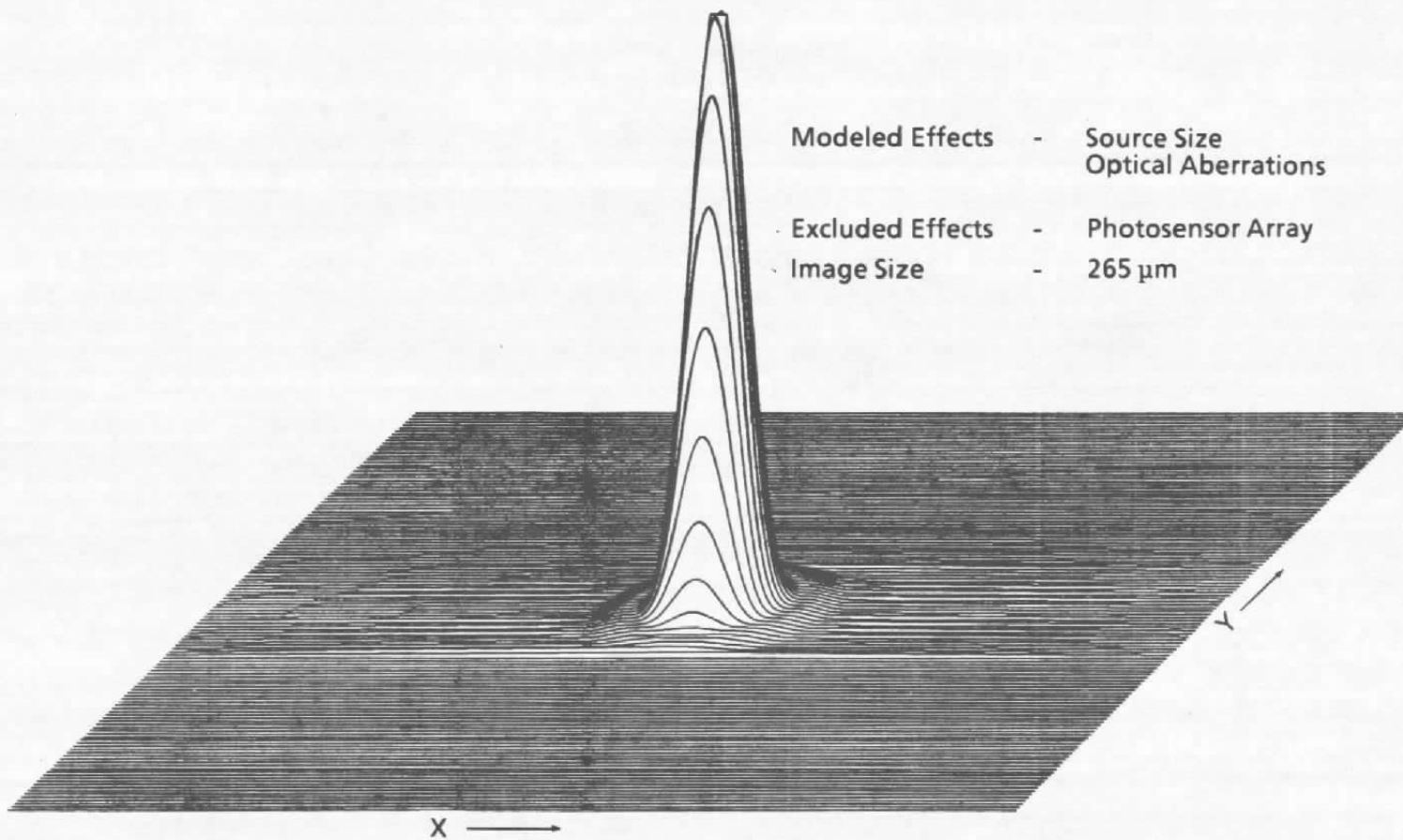
b. Code V[®] image, Model No. 2
Figure 6. Continued.



c. Code V[®] image, Model No. 3
Figure 6. Continued.

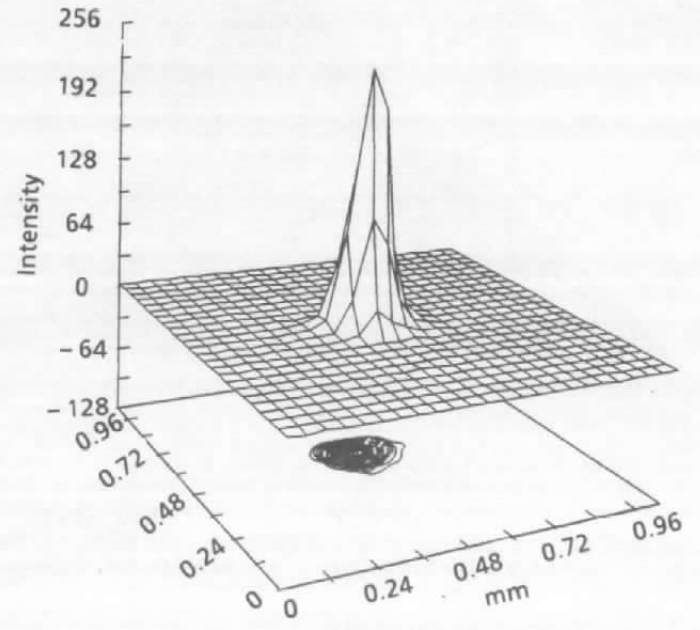
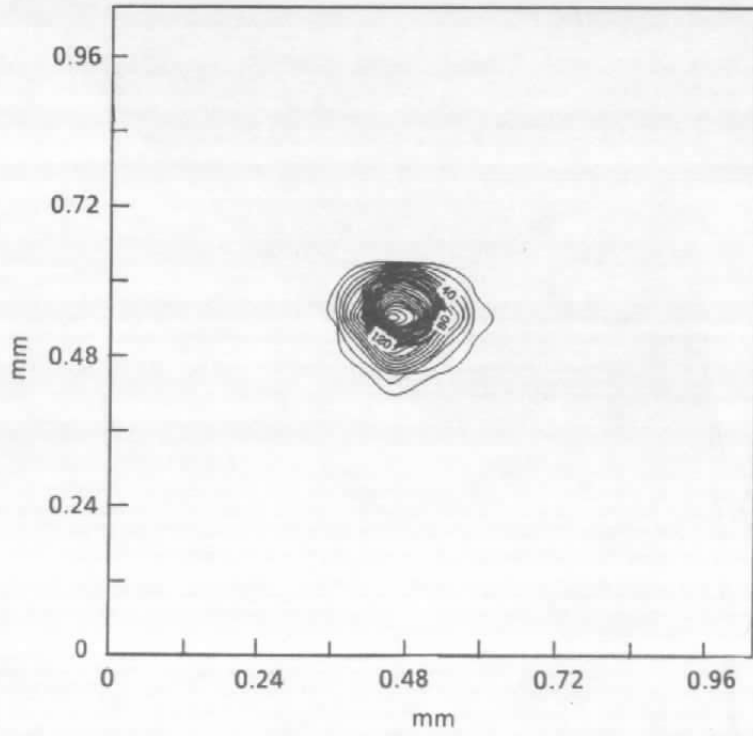


d. Code V[®] image, Model No. 4
 Figure 6. Continued.



e. Code V® image, Model No. 5
Figure 6. Continued.

34



f. Actual image, image size, 263 μm
Figure 6. Concluded.

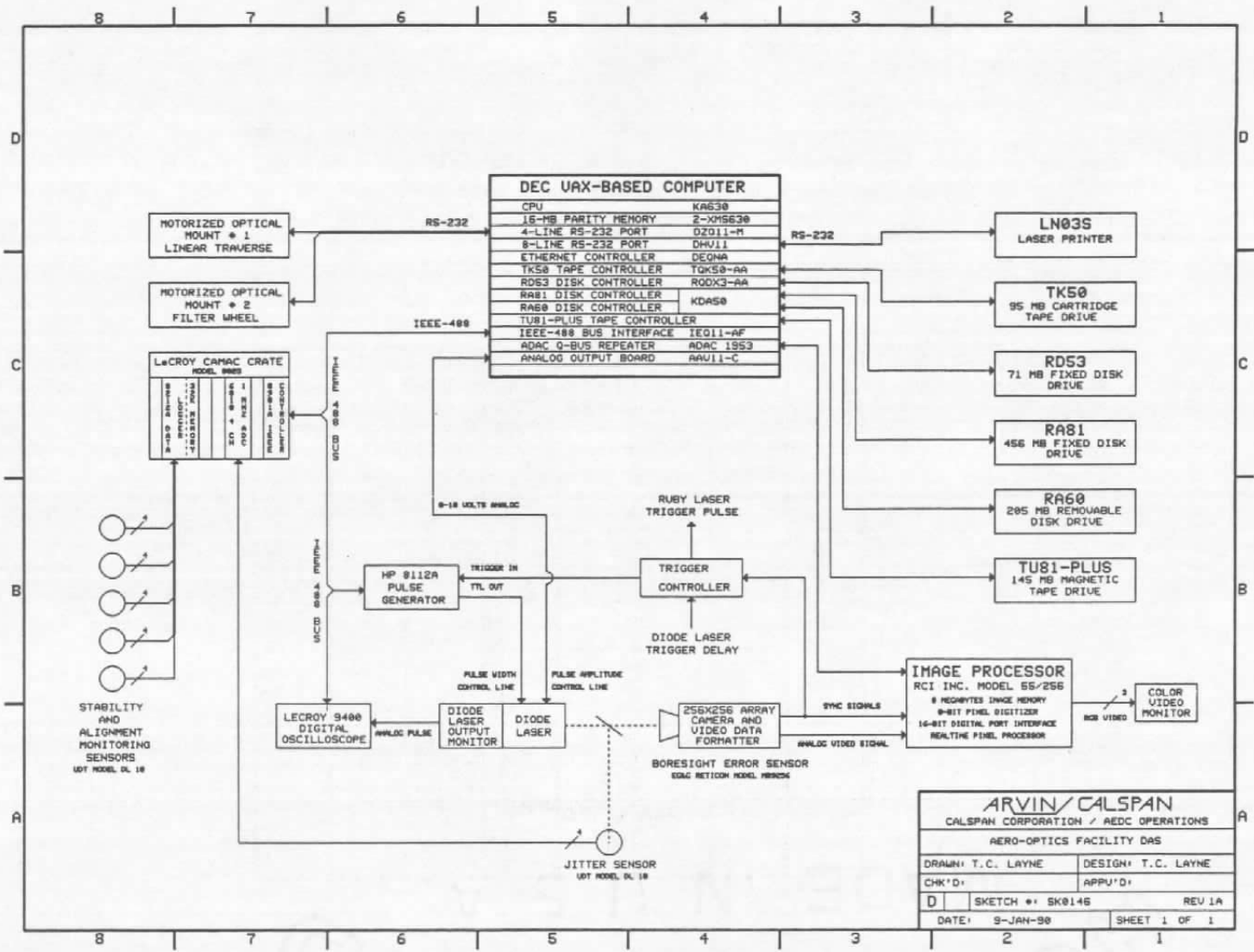
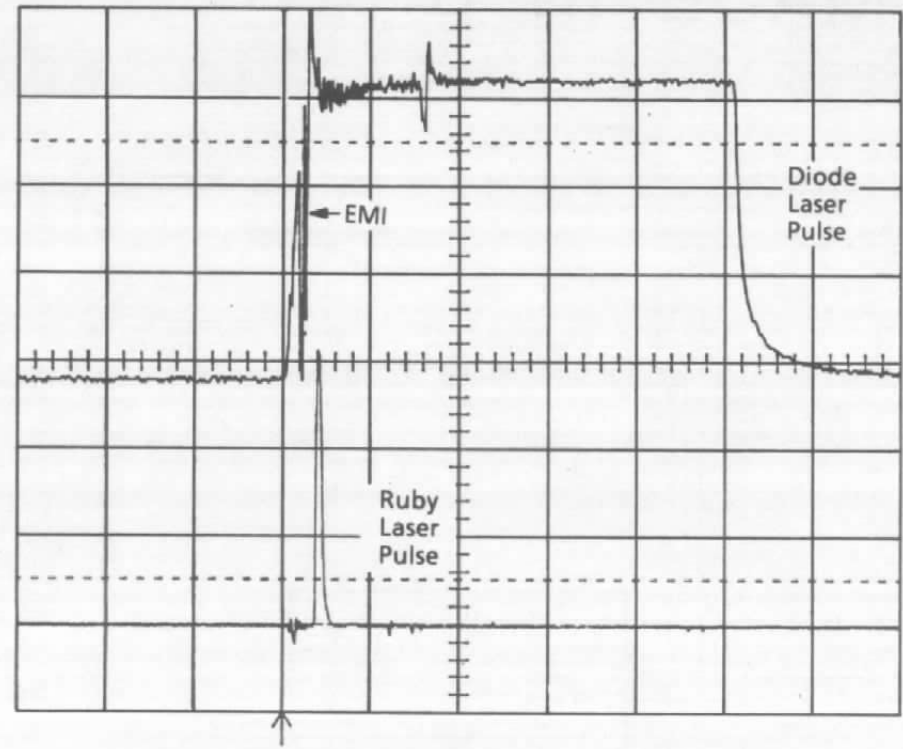
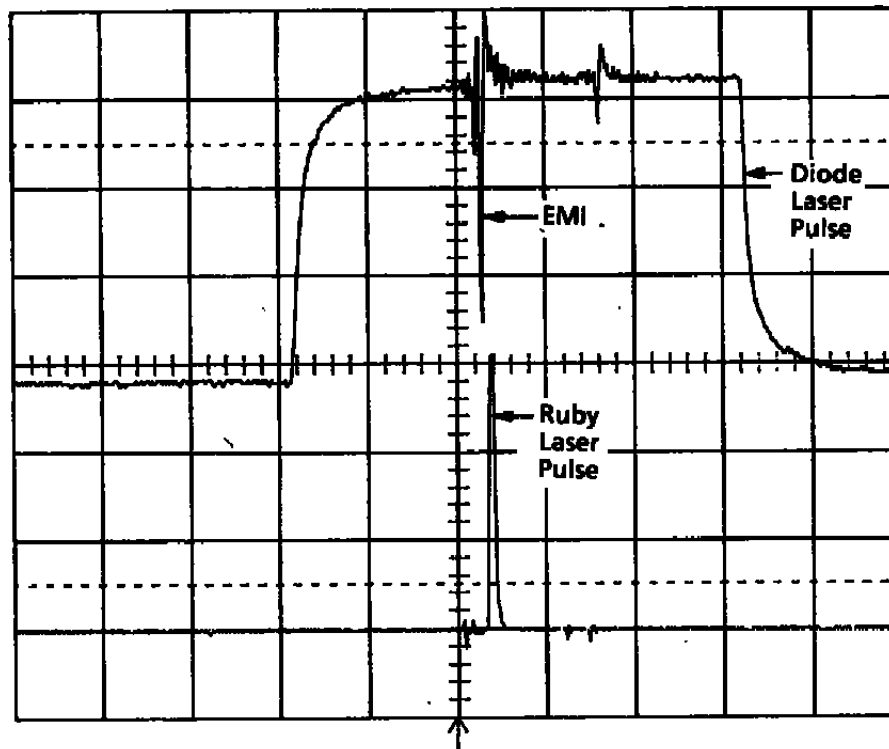


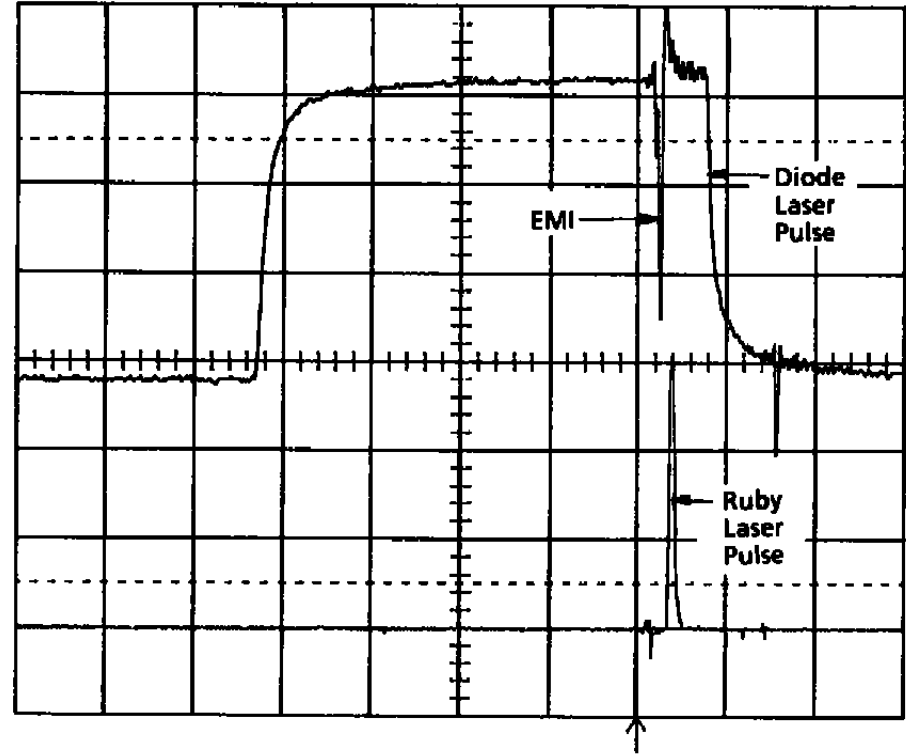
Figure 7. AO data and control system (AO-DACS).



a. Ruby laser pulse at the beginning of the diode laser pulse
Figure 8. Adjustable time synchronization of the diode laser pulse with respect to the ruby laser pulse.



**b. Ruby laser pulse at the midpoint of the diode laser pulse
Figure 8. Continued.**



c. Ruby laser pulse at the end of the diode laser pulse
Figure 8. Concluded.

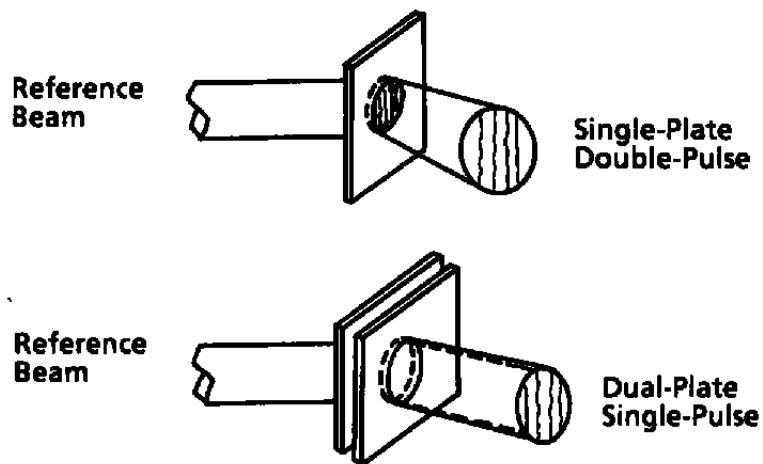


Figure 9. Two types of holographic interferometry.

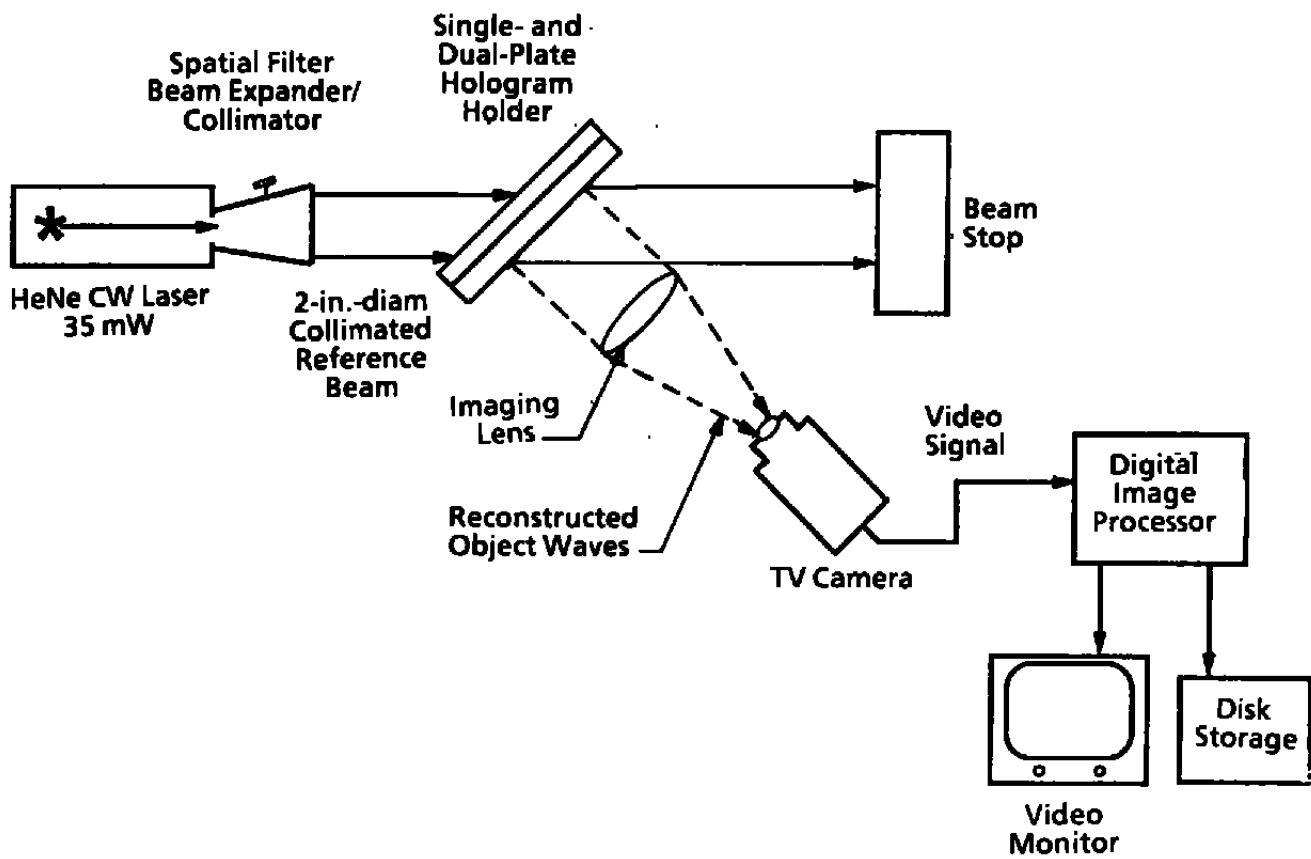


Figure 10. Holographic reconstruction system.

Table 1. Pulse Energy Statistics, 150 Pulses

Pulse Duration, μsec	Maximum/Mean	Minimum/Mean	Standard Deviation/Mean
1.0	1.008	0.991	0.003
10.0	1.004	0.995	0.002
20.0	1.007	0.991	0.004
25.0	1.017	0.992	0.004
30.0	1.007	0.991	0.004
45.0	1.016	0.985	0.006
60.0	1.018	0.988	0.006
90.0	1.009	0.984	0.007
120.0	1.008	0.985	0.006
250.0	1.018	0.988	0.006
750.0	1.029	0.970	0.014

APPENDIX A

OPTICAL PERFORMANCE OF HEATED WINDOWS

The optical performance of fused silica and sapphire windows were compared under identical radiant heating conditions. The results obtained from image quality, sheared wave interferograms, and IR temperature maps showed 1/10th as much image blur growth and wave front distortion as a result of temperature gradients in sapphire as in fused silica. Temperature gradients were less in sapphire because of its higher thermal conductivity. Also, conductive heat flow out of the windows was limited by large contact resistance between the windows and frames, which along with its higher conductivity, accounted for the superior performance of the sapphire under nonuniform heating conditions.

The relative orientations of principal components in the experimental setup are sketched in Fig. A-1. Well-collimated (less than one arc sec divergence) light was transmitted through a window at a 60-deg incidence angle and imaged on an array camera. A rectangular radiant heater was positioned to heat the window from the side opposite the probe light input. An infrared imaging camera viewed the window from the side of the probe light input. Sheared wave interferograms were formed from first and second surface reflections off the window and recorded on a video tape.

Figure A-2 is a typical fused silica window temperature map showing that the heating was symmetric but greater in the center. Similar heating patterns but with much smaller temperature gradients were observed in sapphire. The difference between the central and aperture boundary temperatures was called temperature span. The central peak and temperature span data are plotted in Fig. A-3 for fused silica and sapphire. The more peaked characteristic of the fused silica window caused much more image blur growth for fused silica than for sapphire as is illustrated in Figs. A-4 and A-5. Blur growth in fused silica reached ten times the diffraction limit, whereas blur growth in sapphire reached only twice the diffraction limit. This is consistent with the predictions based upon material thermal properties given in Ref. 4. It is inferred from this result that the contact thermal resistances between the windows, and the frames were so large as to make radiation the dominant cooling mechanism at all elevated temperatures since convection was eliminated by the vacuum conditions inside the test chamber.

Figure A-6 gives the relationship between linear dimension image blur growth and wave front phase shift across the aperture, which is of considerable practical value to the optical engineer when setting up or monitoring optical systems. It shows that the quality of an image can be predicted before the setup is complete by visual inspection of real-time sheared wave interferograms and that corrective action can be taken at opportune times. Figure A-6 also

shows that the blur growth values in sapphire are all in the 1 to 2 range, whereas blur values for fused silica extend up to 10 for identical heater conditions.

Other significant results during this laboratory test series include demonstration of diffraction-limited optical system performance and day-to-day optical axis angular stability within $10 \mu\text{rad}$ using the AO measurement system ultimately to be used for production testing in Tunnel C.

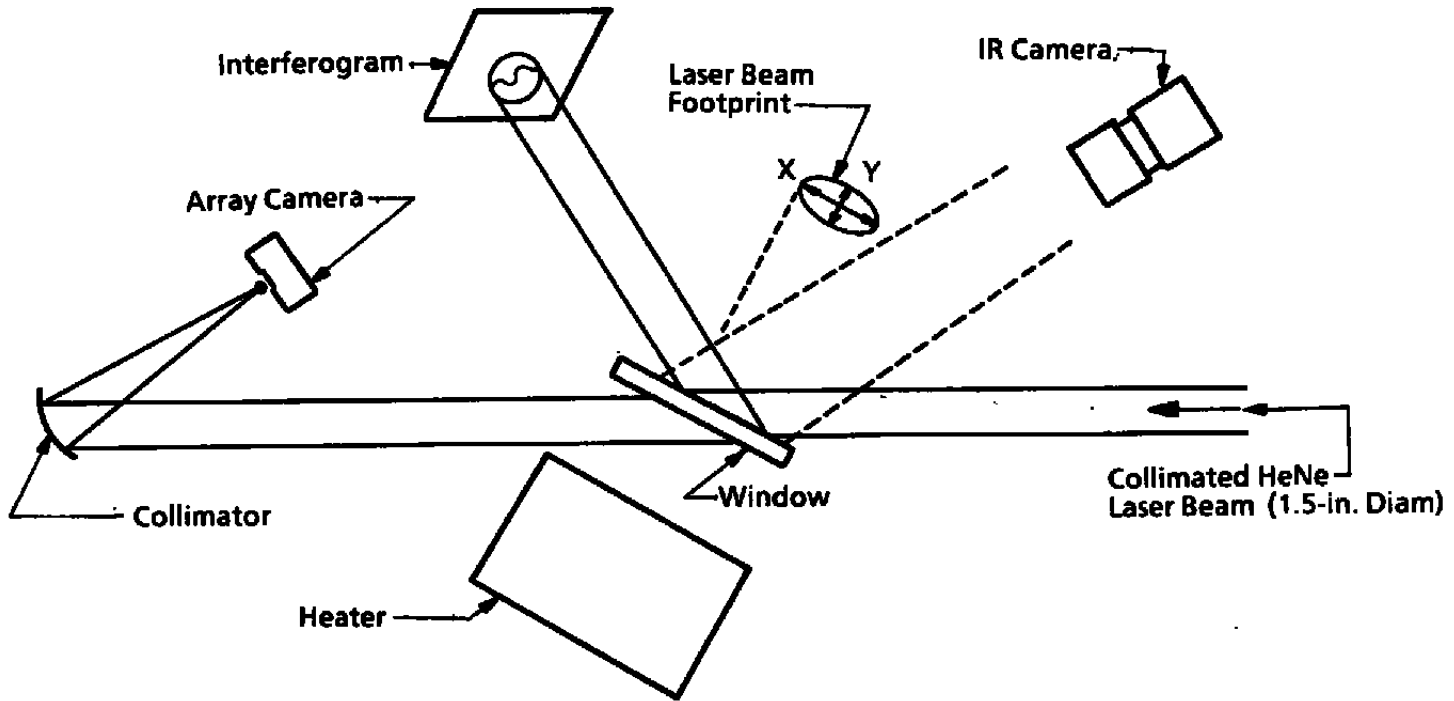


Figure A-1. Heated window optical measurements.

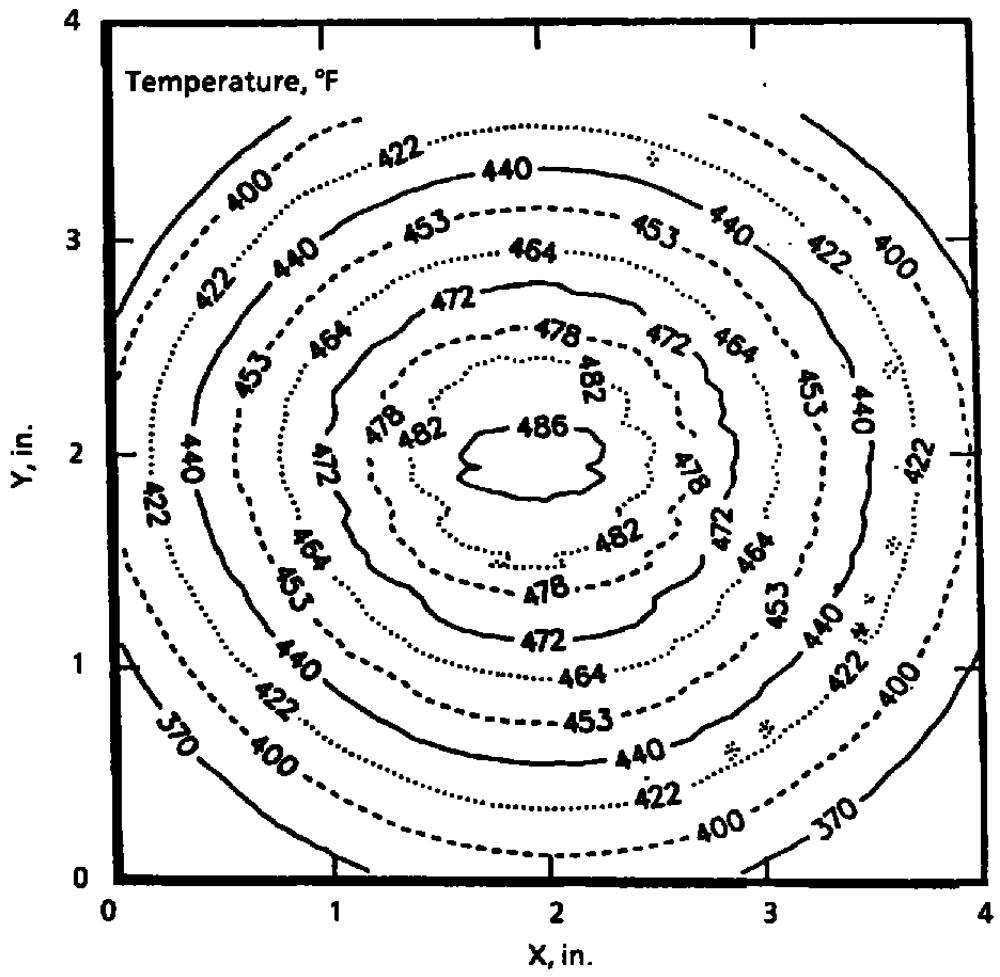


Figure A-2. Typical temperature contour map, fused silica.

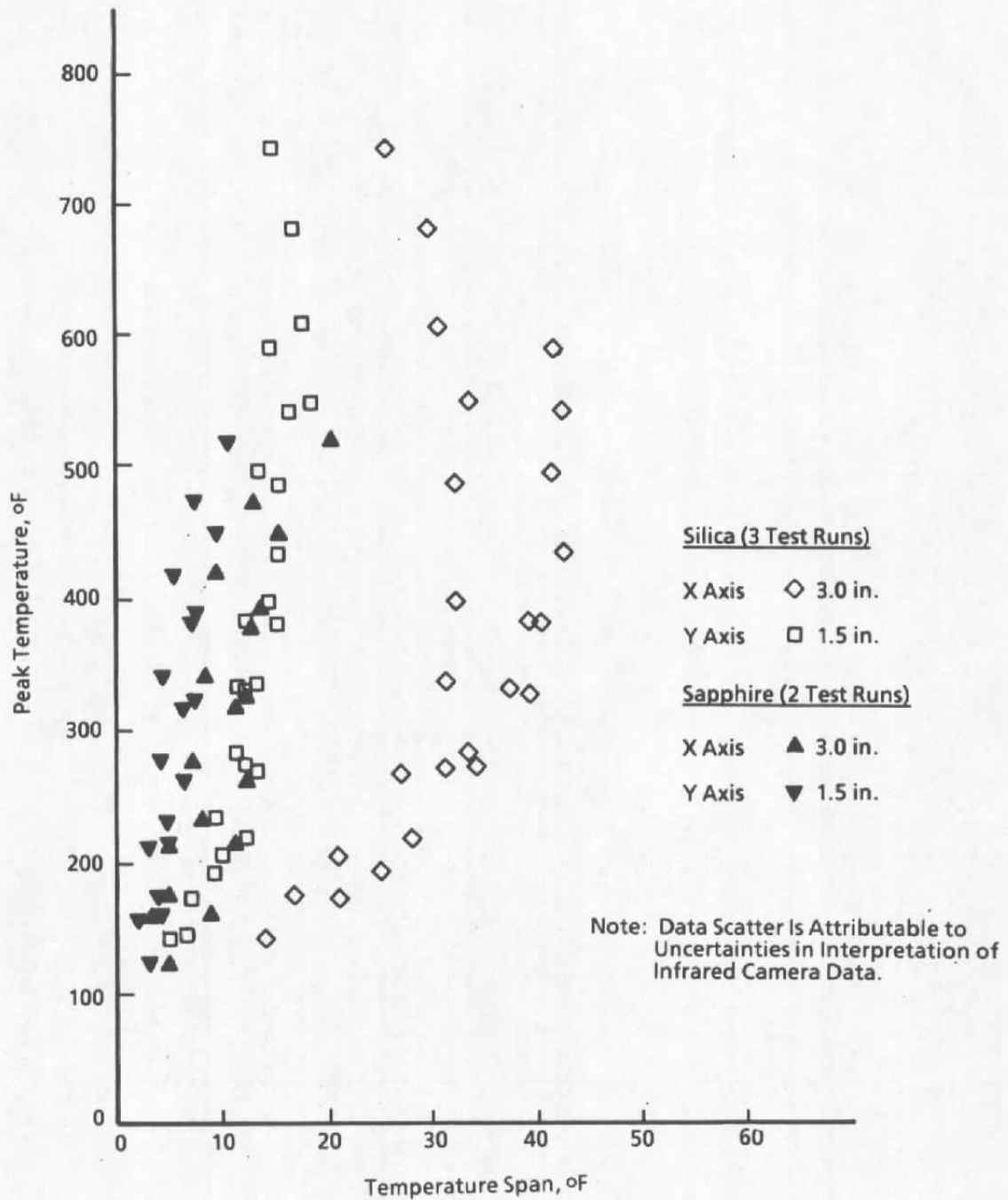


Figure A-3. Temperature spans across laser beam footprint.

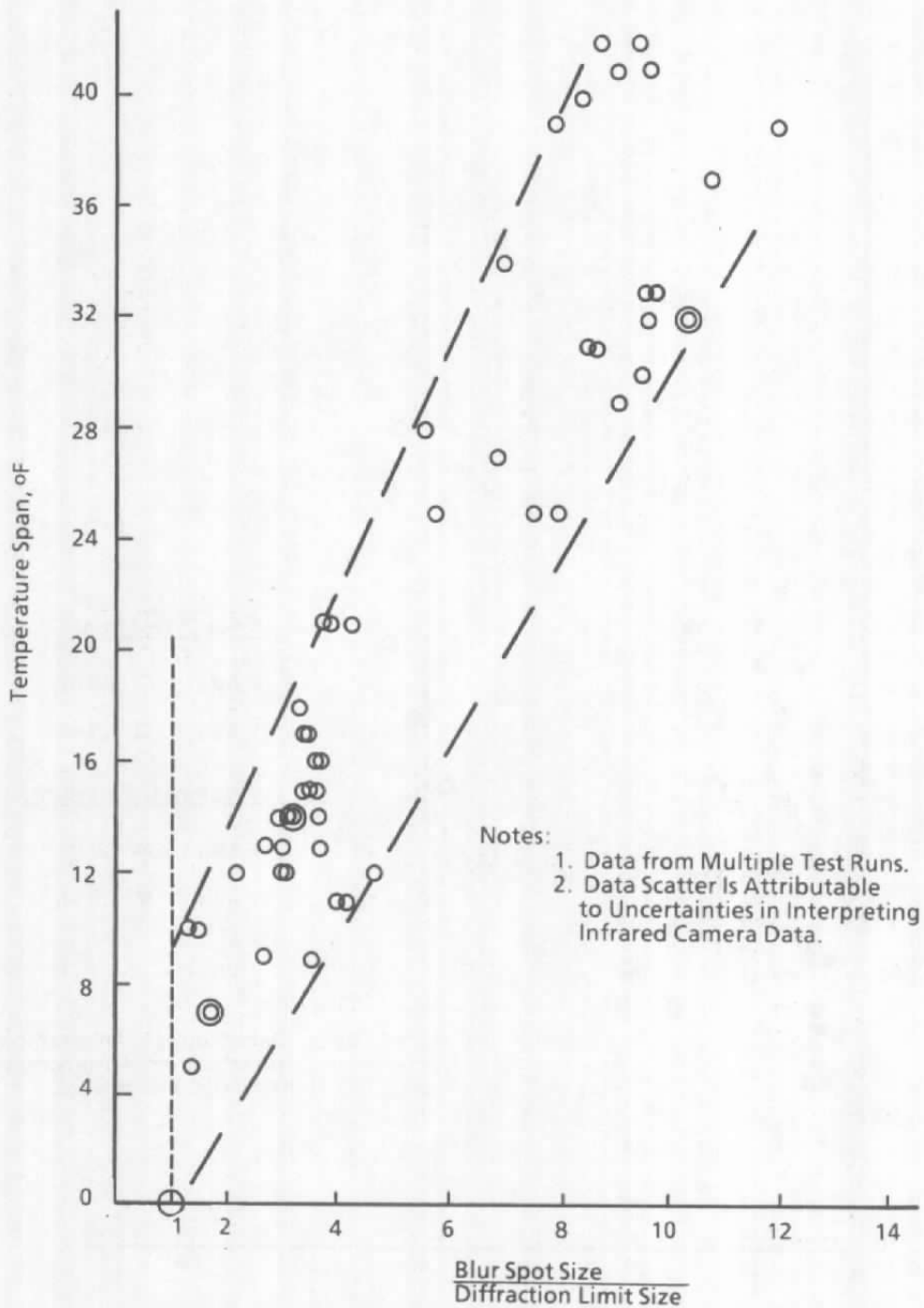


Figure A-4. Blur growth versus temperature span, fused silica.

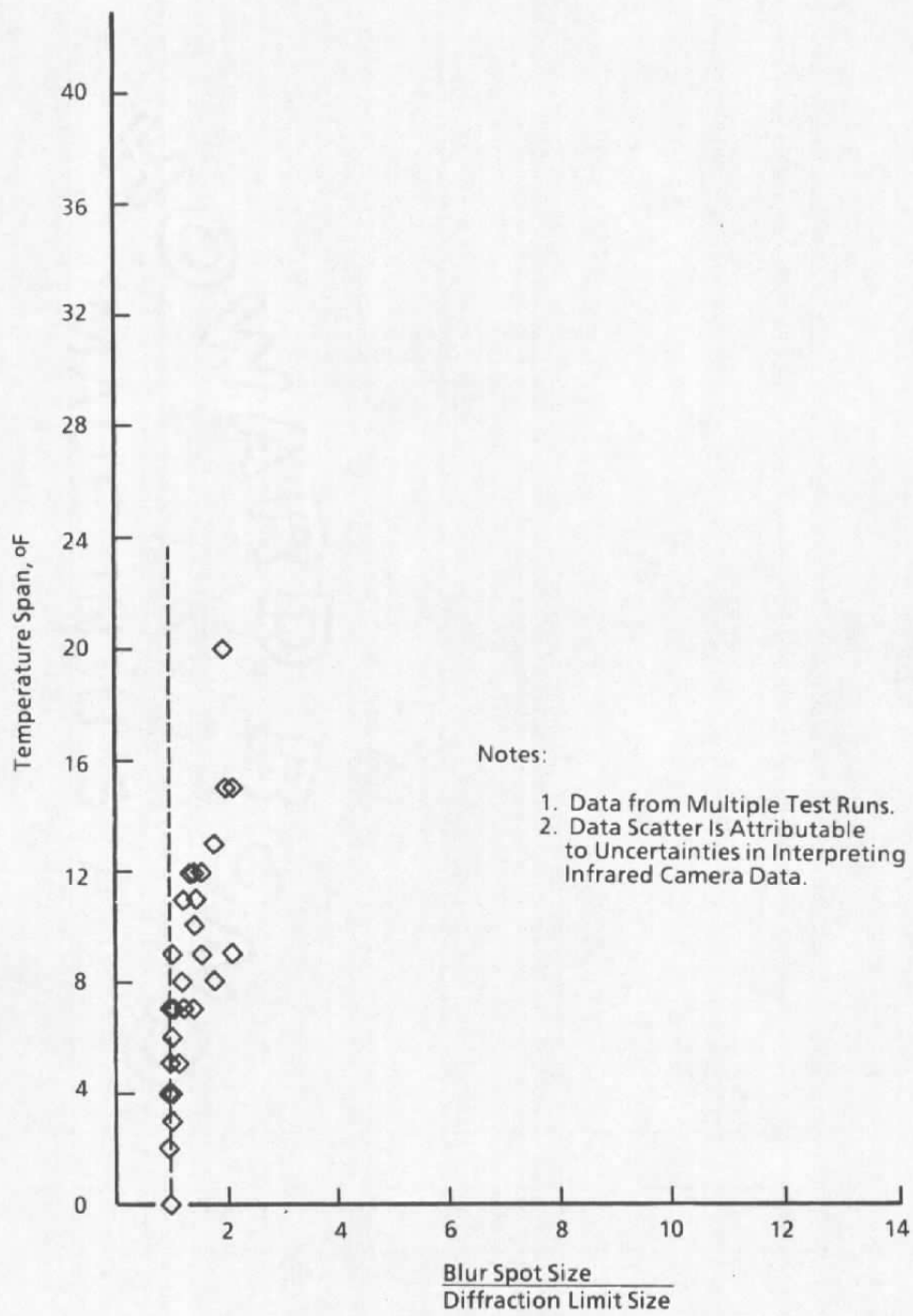


Figure A-5. Blur growth versus temperature span, sapphire.

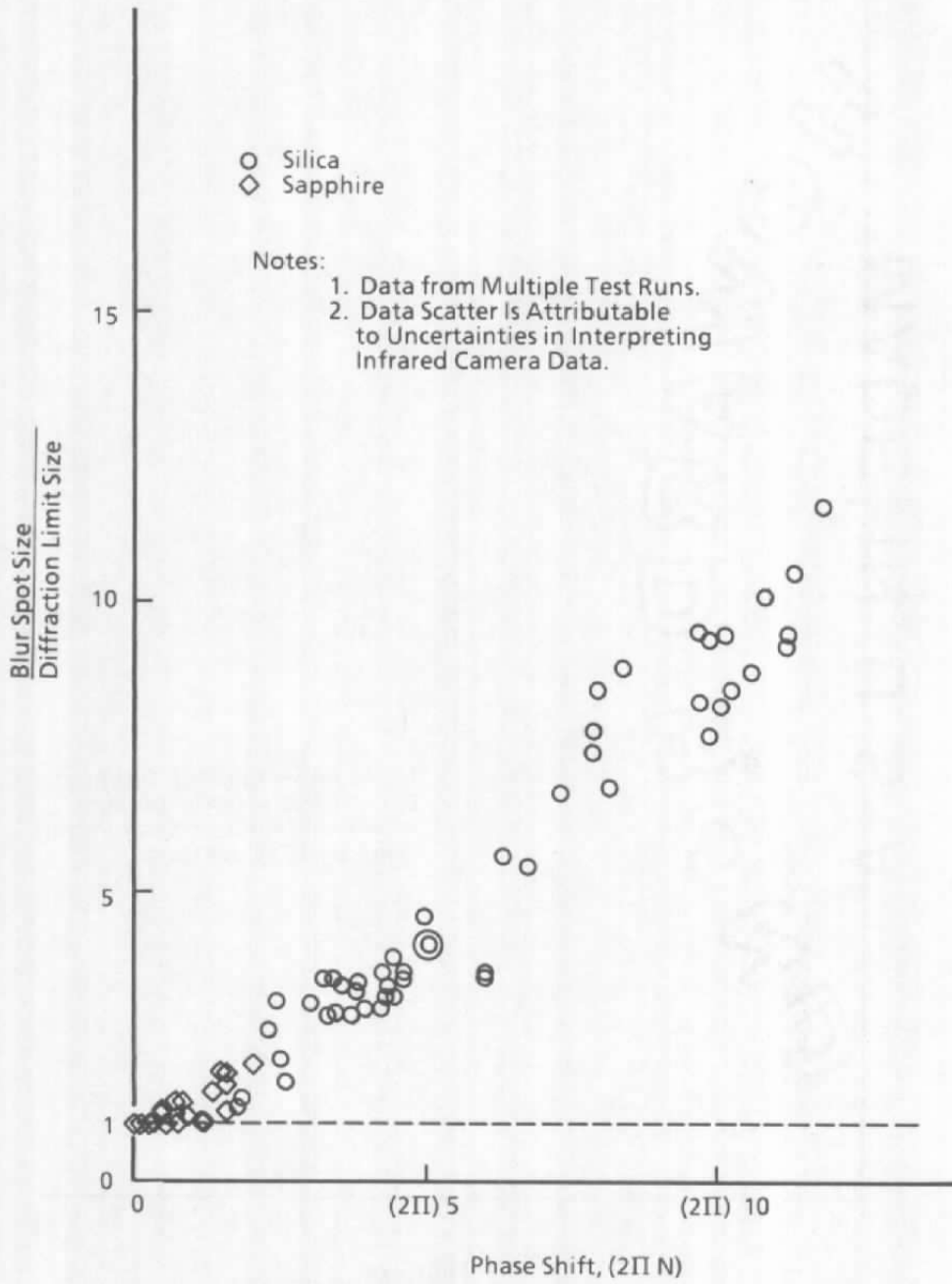


Figure A-6. Blur growth versus wave front phase shift.

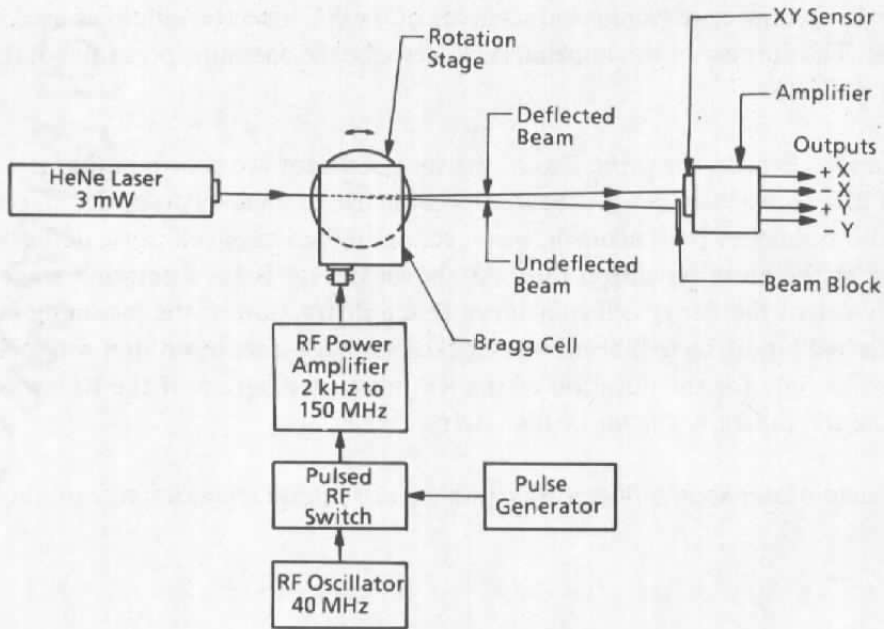
APPENDIX B

DYNAMIC LASER SPOT DEFLECTOR

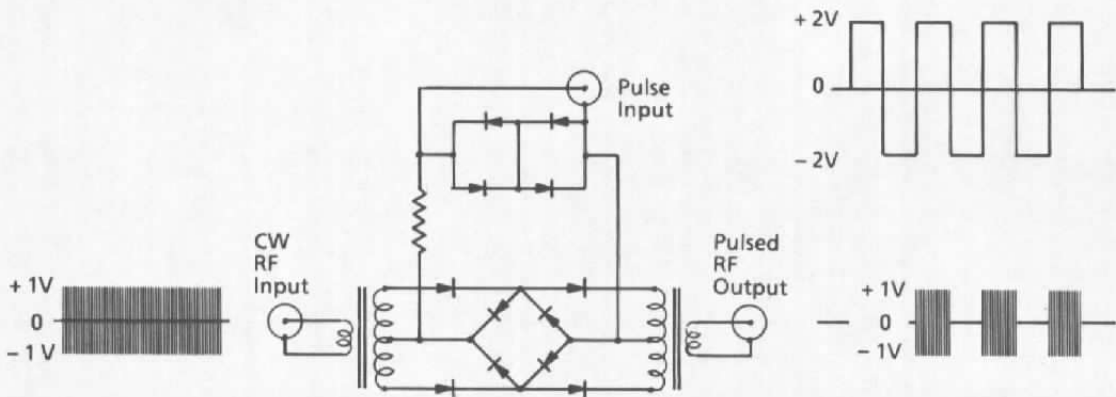
In Section 2.1, a dynamic laser spot deflection scheme was cited as the device used to determine the frequency response characteristic of the XY detector/amplifier used to monitor image jitter. The purpose of this appendix is to describe the operating principles of the dynamic laser spot deflector.

Diagrams to explain the principles of the spot deflector are shown in Fig. B-1. Dynamic deflection of a HeNe laser beam is based upon the use of an acousto-optic cell (Bragg cell). Pulsed radio frequency (RF) acoustic waves set up in the Bragg cell cause deflections of the laser beam at the pulse repetition rate. As shown in Fig. B-1a, a rotation stage was used to properly orient the Bragg cell to achieve Bragg diffraction of the incoming laser beam. The undeflected (undiffracted) beam was blocked so that a laser beam spot was incident upon the XY sensor only for the duration of the RF pulse. A diagram of the RF switch used to produce the RF pulses is shown in Fig. B-1b.

The dynamic laser spot deflector was usable up to a pulse repetition rate of about 2 MHz.



a. Functional diagram



b. Pulsed RF switch

Figure B-1. Dynamic laser spot deflector.

APPENDIX C

HIGH-SPEED IMAGE RECORDING TECHNIQUE

In Section 2.1, the use of an acousto-optic Bragg cell was proposed as the basis of a scheme for increasing the effective image recording rate from the 100 frames/sec basic framing rate of the camera up to the range of 100,000 recorded images/sec. This could be accomplished by recording two or more spatially and temporally separated images per camera frame. Preliminary examinations of several key feasibility issues indicate the applicability of this scheme, and therefore, the advisability of further study. The purpose of this appendix is to document the information generated to date.

To be useful for 100-kHz image recording rates, the Bragg cell scheme has to be able to switch image positions on the planar photosensor array in less than 10 μ sec. Present estimations show that this switching rate is attainable. The accuracy and precision specifications for the spatial separation of images on a single camera frame have to be compatible with the low-level (tens of microradians) image centroid shifts caused by AO effects under wind tunnel test conditions. Until further studies can be conducted, the Bragg cell spatial separation specifications are only presumed to be adequate.

An important and fundamental feasibility concern is the possible image degradation that might be caused by the Bragg cell. The setup shown in Fig. C-1 was used to investigate this possibility. A Bragg cell was attached to an angular rotation stage, and this assembly was retrofitted into the AO measurement system between lenses L3 and L4 (See Fig. 3). The Bragg angle, ϕ , is given by

$$\phi = \frac{\lambda f}{2v} \quad (\text{C-1})$$

where λ is the optical radiation wavelength (830 nm), f is the frequency (40 MHz for this case) of the acoustic waves set up in the Bragg diffraction medium and v (3,900 m/sec for this case) is the acoustic velocity in the Bragg diffraction medium. To satisfy the Bragg relationship of Eq. (C-1), the rotation stage was used to adjust the angular orientation of the Bragg cell with respect to the diode laser beam axis. The drive level of the RF oscillator was then adjusted to produce a power amplifier output of about 1.5 W, which in turn, produced equal intensities of the undiffracted and Bragg diffracted beams at the output of the Bragg cell. A set of 150 frames of array camera data was taken. A typical frame from this set is shown in Fig. C-2, and it can be seen that no significant image degradation is evident.

The optical power in the Bragg diffracted beam is a sensitive function of Bragg cell alignment. Reference C-1 shows that the half-power point of the Bragg diffracted beam is reached at a misalignment angle of $\pm(0.45v)/(2 f L)$ where L is the width of the Bragg interaction medium. Using the design parameters for the Bragg cell used in this investigation (IntraAction Model AOM-405), the allowable misalignment angle specification is found to be about $\pm 800 \mu\text{rad}$. Therefore, the tens of microradians of imaging beam angular fluctuations caused by AO effects are not expected to negate the use of the Bragg cell for image position switching.

Although incomplete, investigations to date have yielded positive indications for the use of a Bragg cell to produce an effective image recording rate in the 100-kHz range.

REFERENCE

- C-1. Gordon, E. I. "A Review of Acousto-optical Deflection and Modulation Devices." *Proceedings of the IEEE*, Vol. 54, No. 10, October 1966.

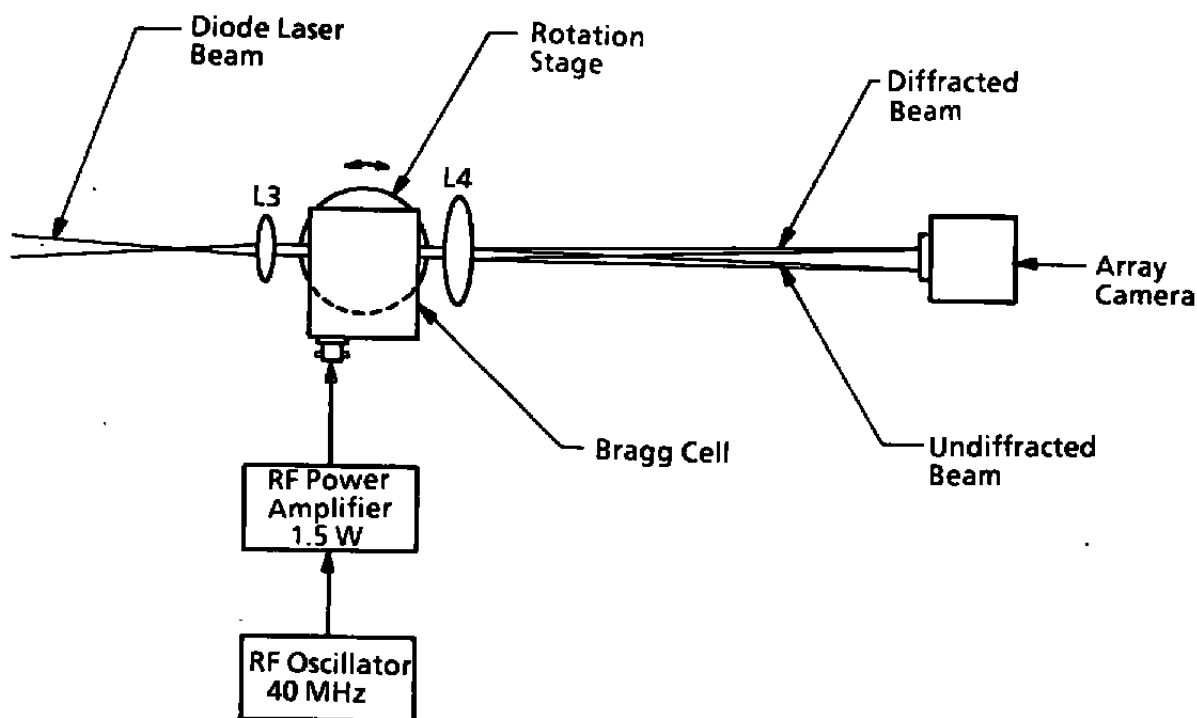


Figure C-1. Bragg cell dual-image generator.

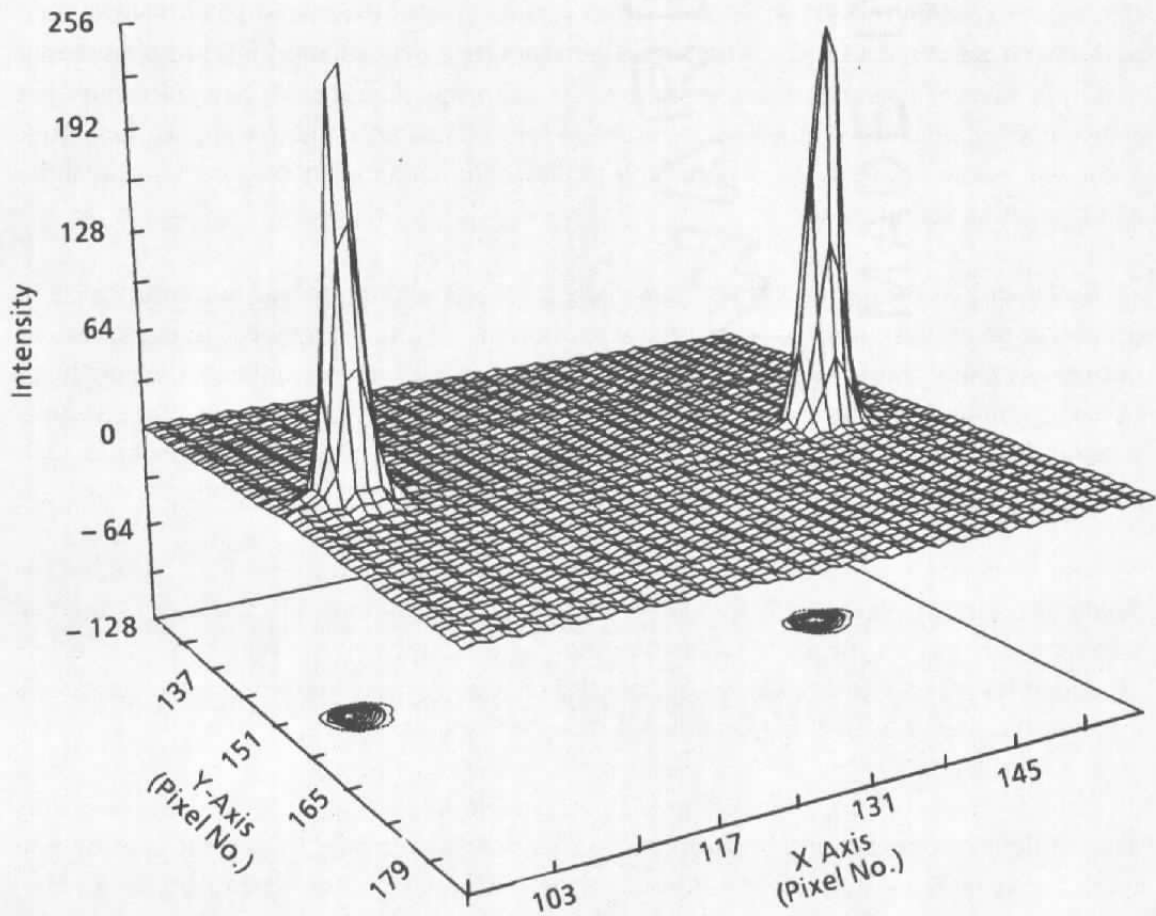


Figure C-2. Dual image produced by the Bragg cell.

APPENDIX D

EVALUATION OF THE INTEGRATING SPHERE TO CHARACTERIZE ARRAY CAMERA RESPONSE NONUNIFORMITY

The purpose of this appendix is to document the results of a first effort to characterize the response nonuniformity of the 256- by 256-array camera (Reticon Model MC9256) used in the AO measurement system. Response nonuniformity is defined as the pixel-to-pixel output variation when the camera photosensor array is uniformly illuminated. Nonuniformity has previously been identified as a possible problem for exacting array camera applications (Ref. D-1), and measurement of AO image centroid shifts in the microradian range certainly qualifies as an exacting requirement.

Specifications for the MC9256 camera quote a "sensor photo response uniformity of ± 10 percent of saturated output at 50 percent of saturation." Although a thorough measurement uncertainty analysis for the AO measurement system has not yet been initiated, the possibility of having nonuniformities of this magnitude represents an area of concern. Therefore, various schemes for characterizing array nonuniformity were considered. The key element in such a scheme is being able to expose each of the 65,536 photosensors to the same photon flux.

One approach would sequentially expose each photosensor to the same light beam, which would be scanned over the array by a two-dimensional acousto-optic diffraction cell. Another scheme would expose the array to the quasi-uniform intensity at the central portion of an expanded laser beam with a Gaussian intensity profile. A particularly attractive approach involves the use of a light source coupled to an integrating sphere.

Published information for commercially available integrating sphere assemblies with integral light source includes uniformity specifications better than 99 percent over output apertures as large as 2 in. for a 6-in.-diam sphere or a uniformity better than 98 percent over a 4-in. aperture for a 12-in. sphere (Ref. D-2). The 12-in. sphere would be ideal for characterization of the MC9256 since the entire camera head could be positioned within the output aperture so that the photosensor array itself could be located at the sphere tangent plane, the ideal location for uniform irradiance. The integrating sphere irradiance uniformity specifications are better than those estimated for the other two schemes previously mentioned, and the sphere approach is simpler to set up and operate. Therefore, an 8-in.-diam integrating sphere was located at AEDC and obtained for evaluation.

The integrating sphere setup is represented in Fig. D-1. A HeNe laser beam was expanded to a 1-in. diam and then projected through the open input port of the integrating sphere. A textured, high reflectivity coating on the inside of the hollow metal sphere causes innumerable reflections of the incoming beam, which ideally, results in a spatially integrated, uniform

irradiance at the output port. Input laser power is adjusted with a circular gradient neutral density filter. Micrometer drives on the XYZ traversing stage permit adjustments of the photometer or camera position with an accuracy of 10 μm . Array camera images are recorded as described in Section 2.2.

In preparation for use of the integrating sphere, a photometer was scanned across the sphere output to determine the uniformity of the irradiance field. This was done by first positioning the geometric center of the camera array at the nominal geometric center of the sphere output port; this XY position was defined as the $X = 0$ and $Y = 0$ reference coordinate points. Next, the camera was removed, and the photometer head was mounted to the XYZ traverse so that the photometer could be traversed in the XY plane and thereby map out the irradiance characteristics for various positions in the Z-axis direction. To achieve good spatial resolution, a 400- μm pinhole aperture was placed in front of the normal 2-cm entrance aperture of the photometer. Next, the pinhole with attached photometer head was nominally located at the $X = 0$, $Y = 0$, and $Z = 0$ positions, where $Z = 0$ is defined as that Z position where the thin disk holding the pinhole just makes mechanical contact with the planar surface of the output port flange.

Information about the variation of output irradiance versus XYZ position was obtained by manually scanning the photometer/pinhole in the X-axis direction for three Y-axis positions ($Y = 0$, $Y = 5$, and $Y = -5$ mm) and two Z-axis positions ($Z = 0$ and $Z = -14$ mm). The resultant data are shown in Fig. D-2.

As might be expected, irradiance uniformity is seen to degrade rapidly from the $Z = 0$ position to the $Z = -14$ -mm position. Also, the $Z = 0$ position is about 12 mm from the tangent plane at the sphere inner surface because of the flange assembly at the sphere output port. Even so, at the defined $Z = 0$ position, the peak-to-peak irradiance variation along the X-axis is only about 2.9 percent, whereas the peak-to-peak variation along the Y-axis is only about 2.2 percent.

As indicated in Fig. D-1, the camera planar array is recessed inside the camera body by about 5 mm, so that the irradiance nonuniformity would be expected to be somewhat worse for the camera body just contacting the sphere output port flange than for the photometer/pinhole just contacting this same flange ($Z = 0$ position).

For this first look at response nonuniformity, data from only nine camera pixels and three camera positions were examined. The specific pixels are identified in Fig. D-3 by their row and column locations. The three camera positions with respect to the geometric centerline of the sphere output port are also indicated in Fig. D-3. Ten frames of camera data were recorded at each of the three camera positions. The three camera positions and nine specific

pixels permitted five Y-axis (vertical) positions to be sampled as summarized in Table D-1. The minimum and maximum gray-level value for each pixel sample set was plotted as shown in Fig. D-4. The observed 2-percent droop in the irradiance profile from the $Y = 0$ to the $Y = \pm 4.72$ -mm positions is in good agreement with the photometer/pinhole data. At this point in the study, it was encouraging to observe the small, ± 1 -percent pixel-to-pixel variability at each Y position; these data show a better response uniformity characteristic than the manufacturer's specifications indicate.

Since the data shown in Figs. D-2 and D-4 represent only a sparse sampling of the integrating sphere irradiance field and the array camera pixel field, it was decided that more information about the integrating sphere and array camera characteristics was needed. For this purpose, three different Reticon Model 9256 array cameras were obtained and tested with the integrating sphere. A complete frame (256 lines) of analog video data was recorded by a digital sampling oscilloscope for each camera at nominally 50 and 85 percent of each camera's saturation level. The 50-percent saturation level data are shown in Fig. D-5. Variations as large as ± 3 percent are observed; however, some of this variability can be attributed to the oscilloscope sampling process. The 85-percent saturation data are shown in Fig. D-6, and it can be seen that camera No. 1 definitely has a response uniformity problem since the response from about line (row) 200 to line 256 trends down to a level that is about 16 percent low compared to the rest of the lines. This particular camera was rotated by 90, 180, and 270 deg, and each time the frame data were qualitatively the same as shown in Fig. D-6a.

This brief study has shown that a light source coupled to an integrating sphere is a simple and very useful scheme for characterizing array camera response nonuniformity. This study also showed that array cameras should be thoroughly characterized with regard to response nonuniformity over a range of illumination levels before being used in an AO measurement system.

Toward the end of this study, software was developed for the AO data acquisition system to permit generation of a 256 by 256 correction matrix for implementing a more uniform effective response characteristic. However, this capability will not be put to use until a better integrating sphere system is obtained since observed irradiance level uncertainties attributable to the presently used integrating sphere system are as large as observed camera response variations. Reviews of manufacturer's literature indicate that better integrating sphere systems are commercially available.

REFERENCES

- D-1. Tanaka, S. C. "A Need and Method for Nonuniformity Correction in Solid State Image Sensors." *Focal Plane Methodologies III*, SPIE Conference Proceedings, Vol. 350, San Diego, California, August 24-25, 1982.
- D-2. "Integrating Sphere Instrumentation." Labsphere Technical Notes, Labsphere, Inc., P. O. Box 70, North Sutton, New Hampshire 03260.

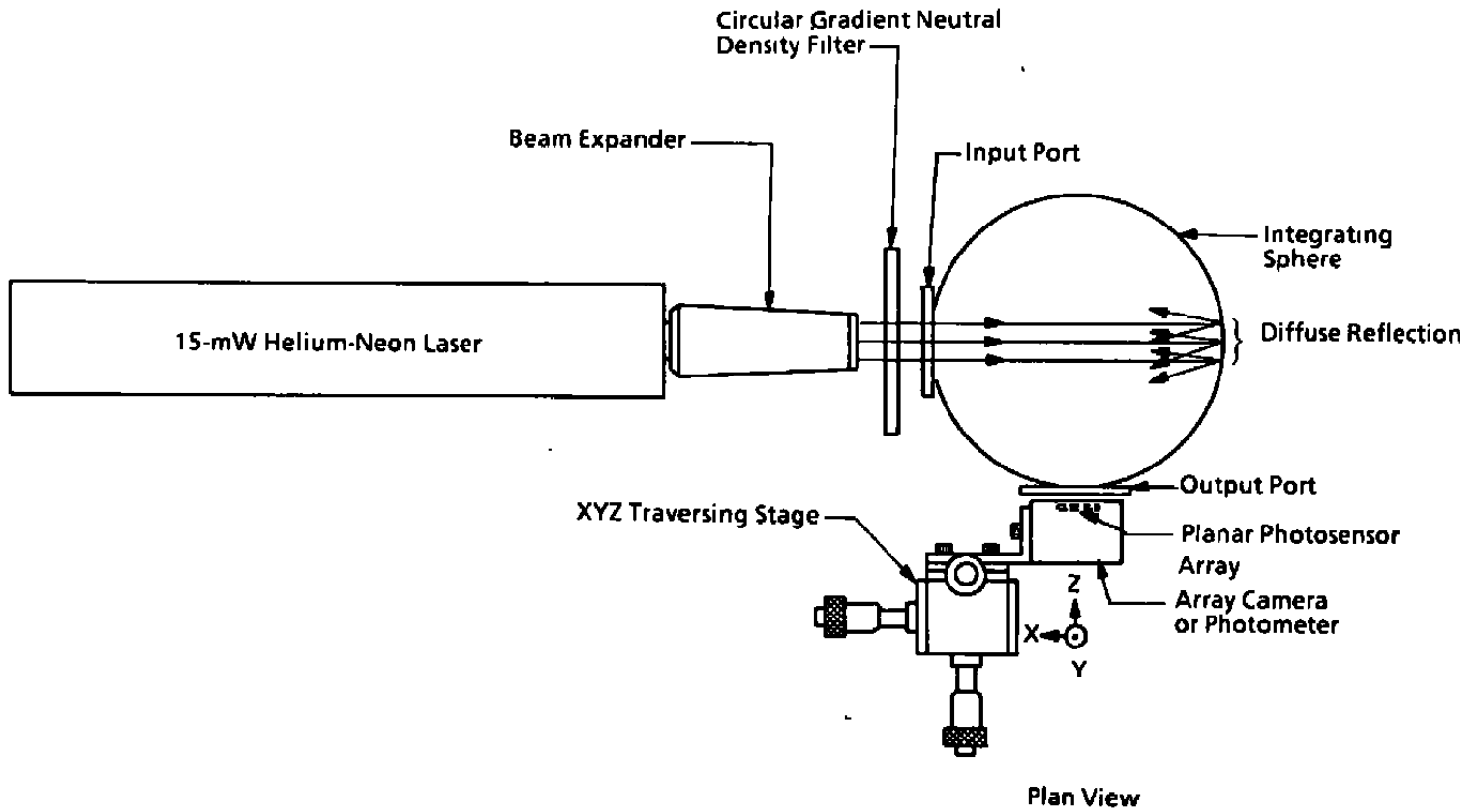


Figure D-1. Integrating sphere setup for characterizing array camera response nonuniformity.

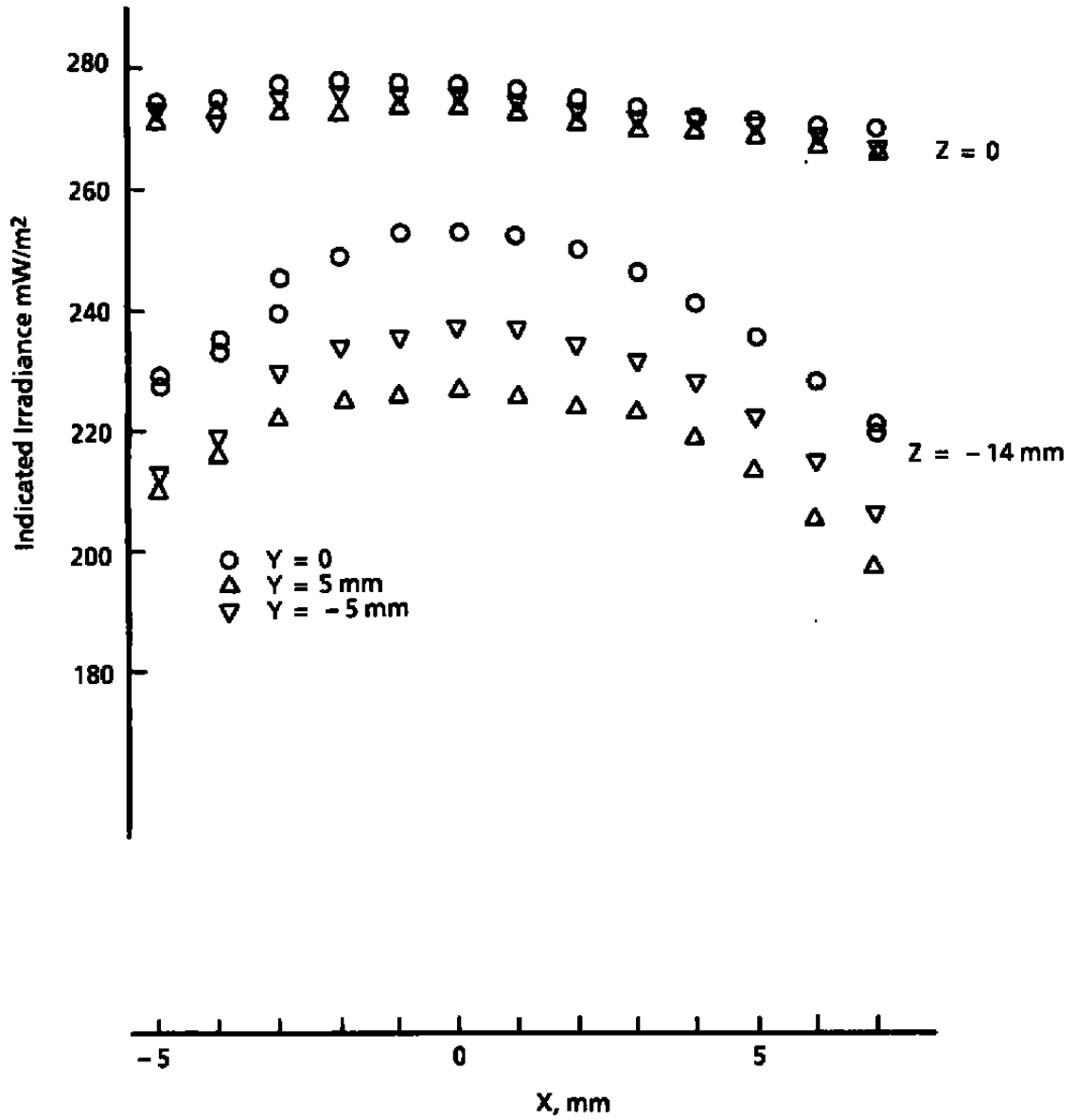
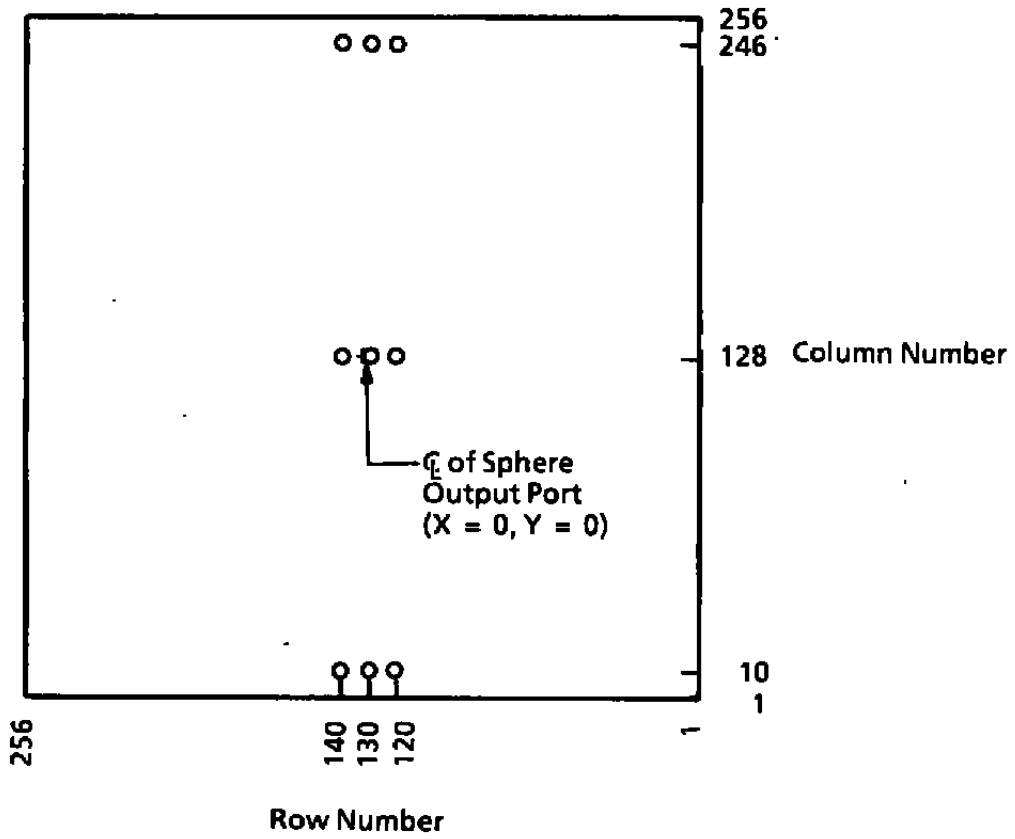
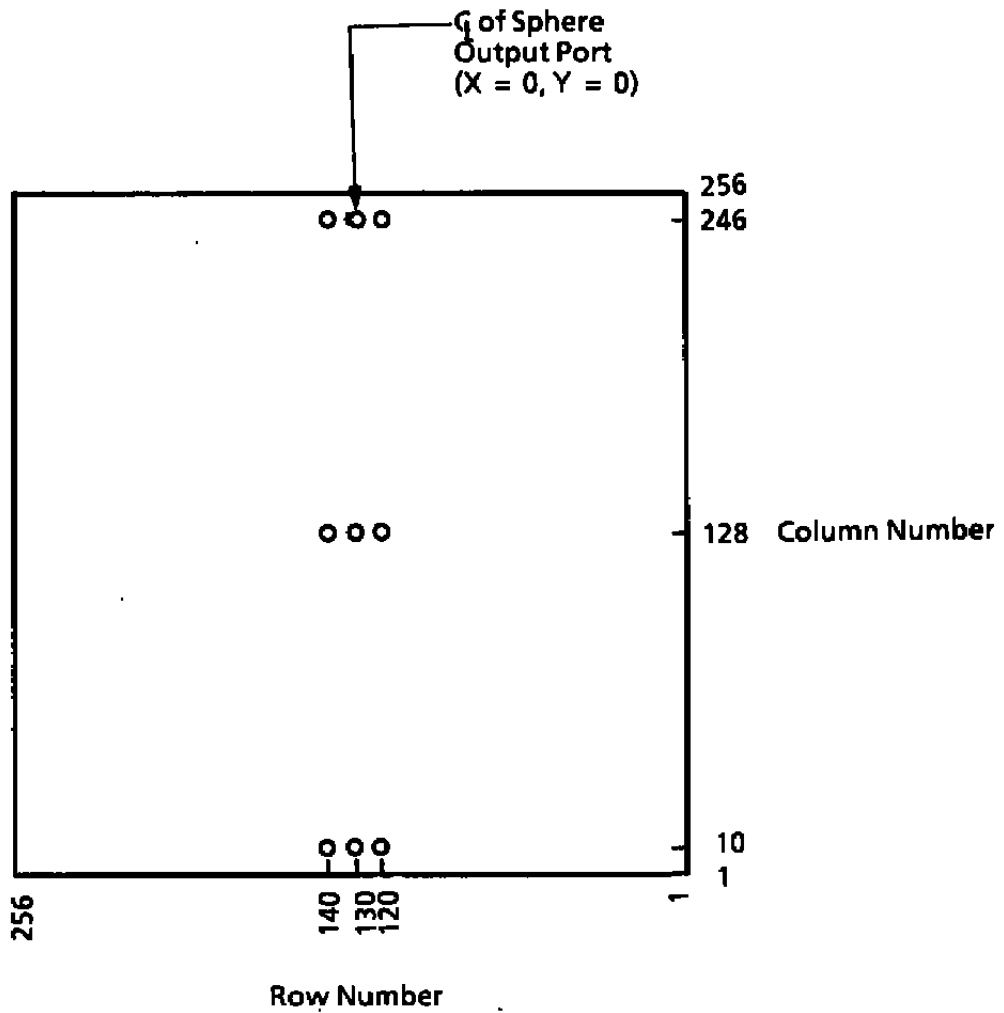


Figure D-2. Photometer/pinhole survey of sphere output.

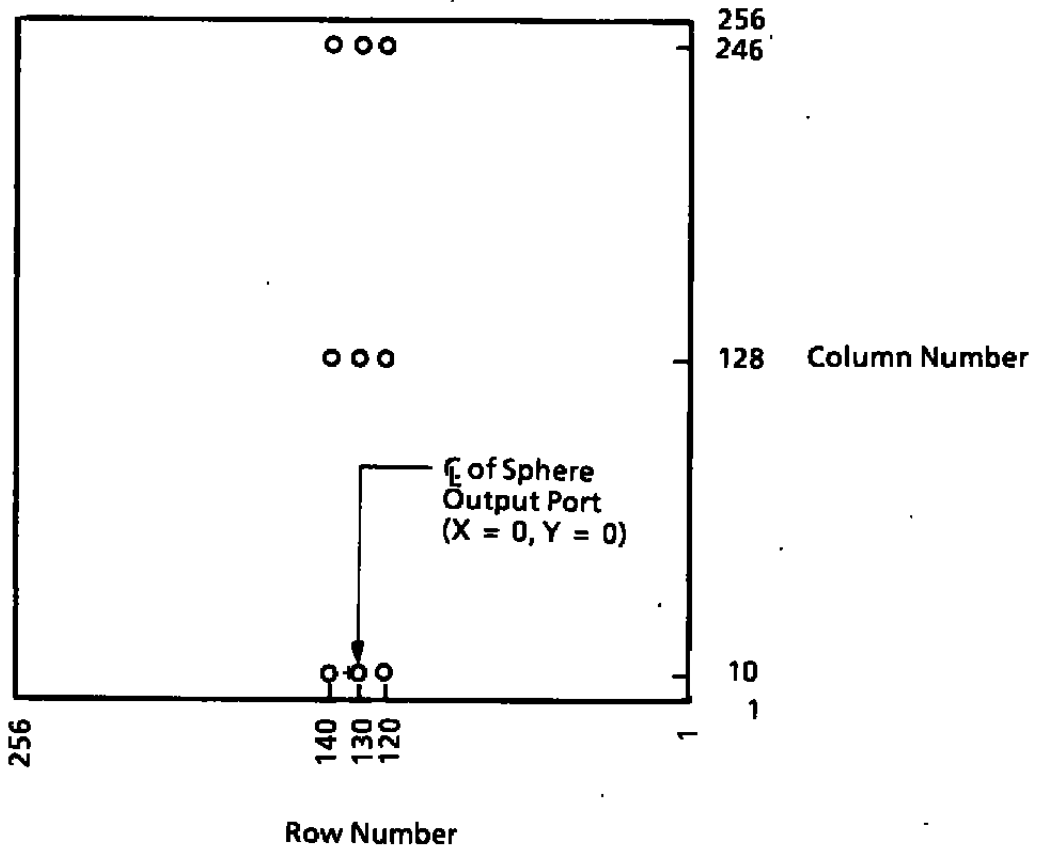


a. Camera position No. 1

Figure D-3. Array camera positions for characterizing response nonuniformity.



**b. Camera position No. 2
Figure D-3. Continued.**



**c. Camera position No. 3
Figure D-3. Concluded.**

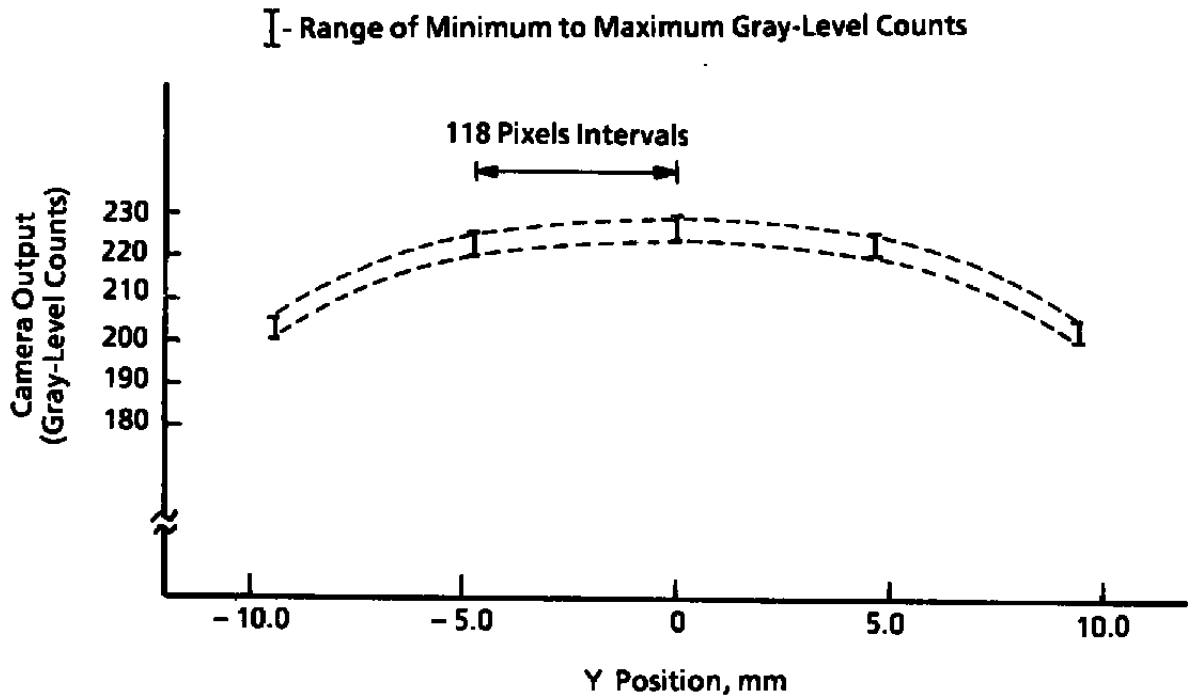
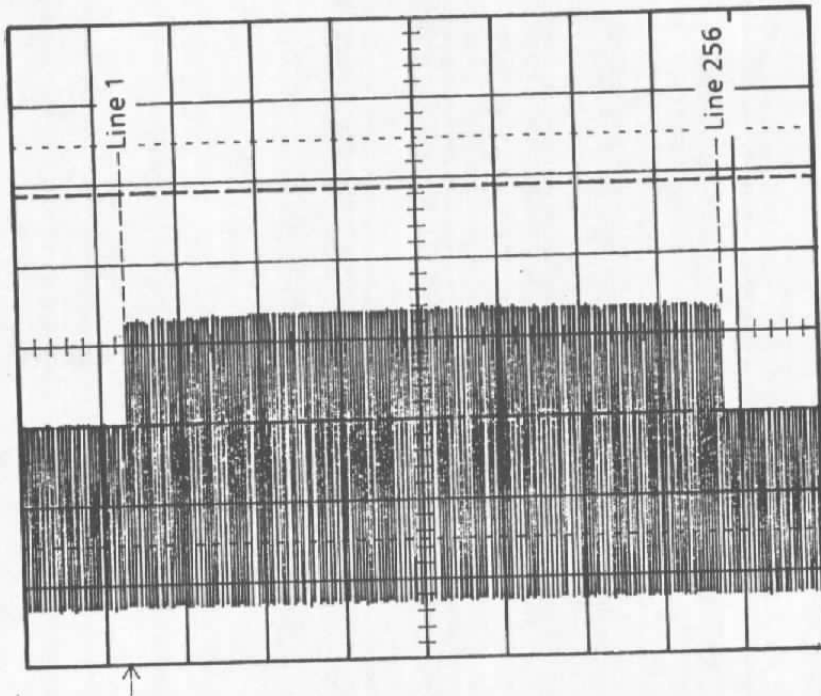
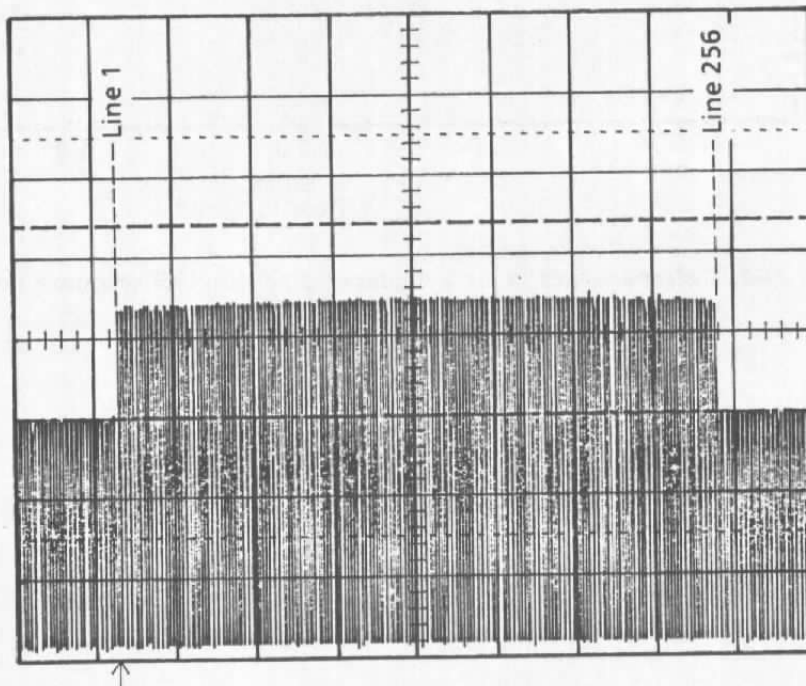


Figure D-4. Determination of array camera pixel-to-pixel response nonuniformity.

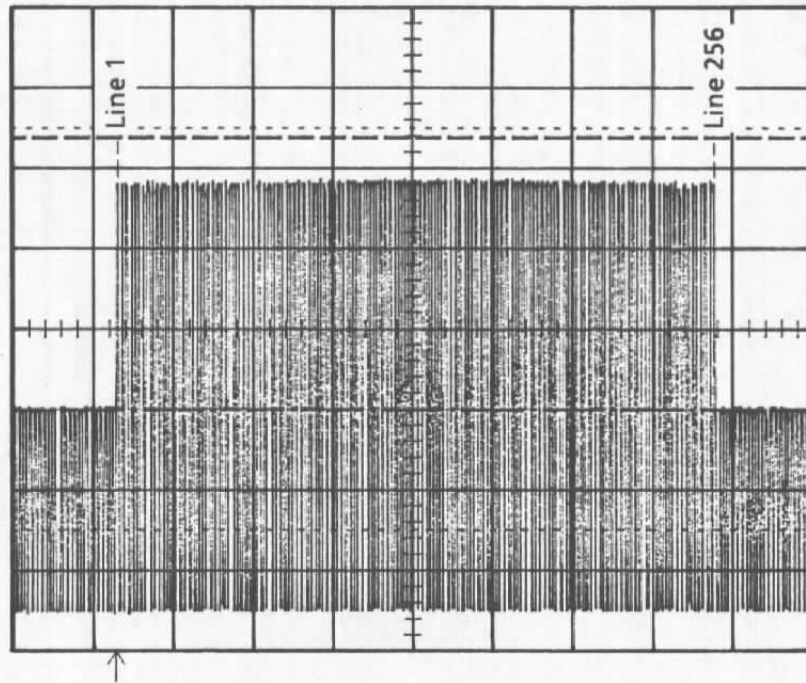


a. Camera No. 1 analog video

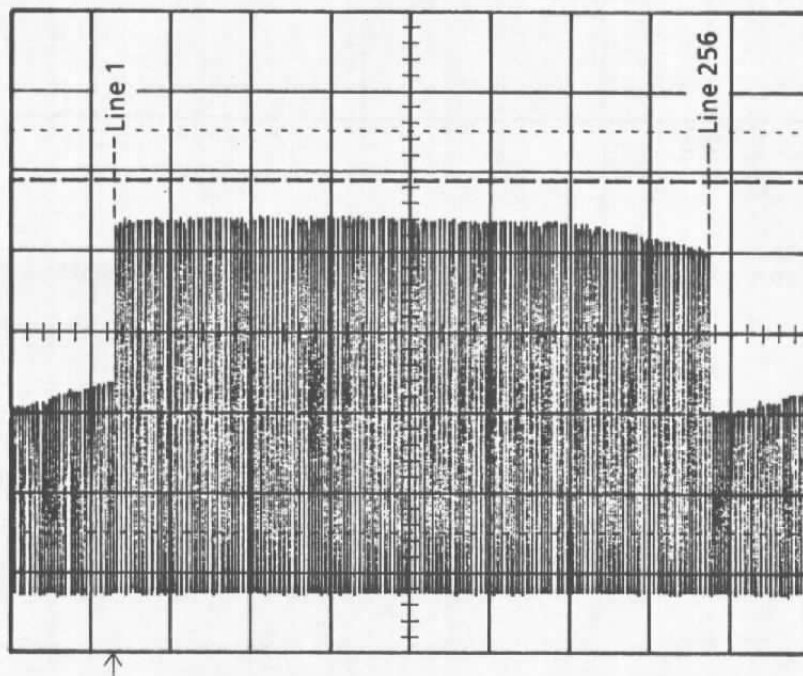


b. Camera No. 2 analog video

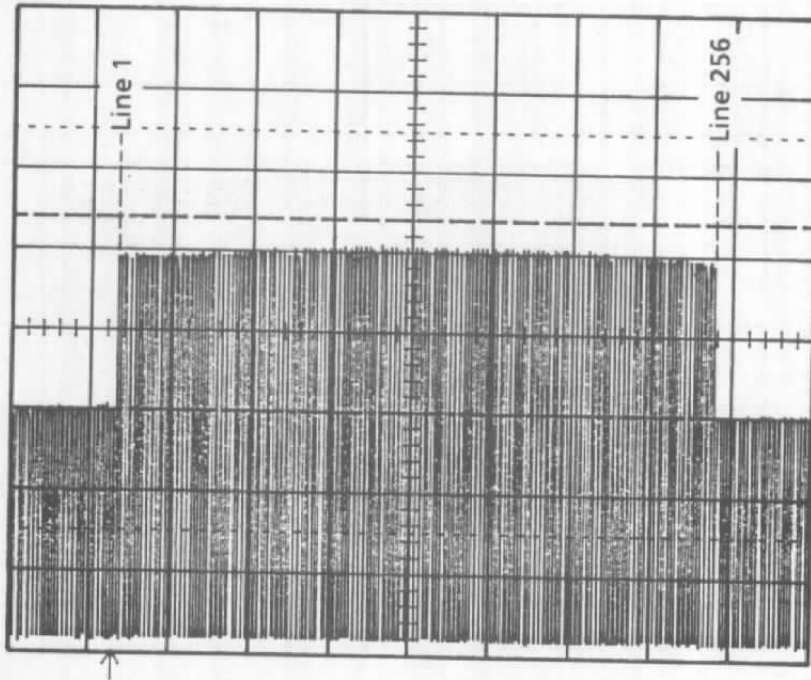
Figure D-5. Response nonuniformity characteristics at a nominal 50-percent saturation level.



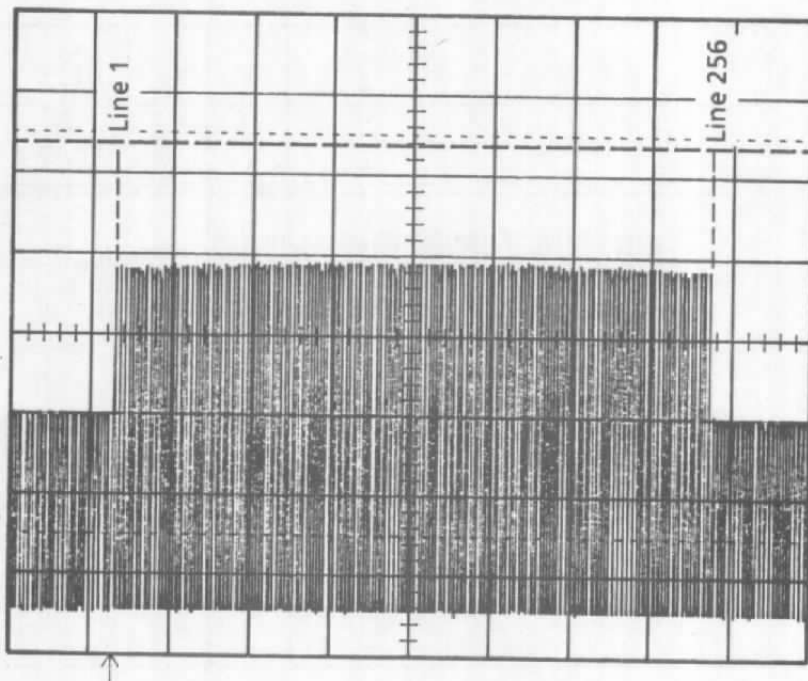
**c. Camera No. 3 analog video
Figure D-5. Concluded.**



**a. Camera No. 1 analog video
Figure D-6. Response nonuniformity characteristics at a nominal 85-percent saturation level.**



b. Camera No. 2 analog video



c. Camera No. 3 analog video
Figure D-6. Concluded.

Table D-1. Pixel Sample Sets

Y Position	Camera Position	Pixel Identification Row, Column
- 9.44 mm	1	None
	2	120,10 10 Frames 130,10 10 Frames 140,10 10 Frames
	3	None
	Total Number of Pixel Samples, 30	
- 4.72 mm	1	120,10 10 Frames 130,10 10 Frames 140,10 10 Frames
	2	120,128 10 Frames 130,128 10 Frames 140,128 10 Frames
	3	None
	Total Number of Pixel Samples, 60	
0	1	120,128 10 Frames 130,128 10 Frames 140,128 10 Frames
	2	120,246 10 Frames 130,246 10 Frames 140,246 10 Frames
	3	120,10 10 Frames 130,10 10 Frames 140,10 10 Frames
	Total Number of Pixel Samples, 90	
4.72 mm	1	120,246 10 Frames 130,246 10 Frames 140,246 10 Frames
	2	None
	3	120,128 10 Frames 130,128 10 Frames 140,128 10 Frames
	Total Number of Pixel Samples, 60	
9.44 mm	1	None
	2	None
	3	120,246 10 Frames 130,246 10 Frames 140,246 10 Frames
	Total Number of Pixel Samples, 30	

APPENDIX E

INITIAL EXAMINATION OF SUBPIXEL CENTROIDDING CONSIDERATIONS

The low-level AO effects expected under wind tunnel testing conditions lead to concern about the centroid resolution capability that may be attained by an AO measurement system. In general, a subpixel resolution capability is desirable. A cursory look at the question of subpixel resolution leads to the conclusion that, ideally, the array camera photosensors should be small and square with uniform responsivity and large fill factor.

An algorithm for subpixel centroiding will have to account for photosensor shape, dimensions, spacing, fill-factor, and interpixel and intrapixel response uniformity. As a first step in developing a subpixel centroiding capability, the focal plane array of the MC9256 camera was probed with a focused HeNe laser beam to determine photosensor shape and dimensions. The probing laser beam diameter at focus was about 5 μm . Specification literature for the camera was not clear as to photosensor shape, although a square shape had been assumed.

Initial probing of the focal plane array indicated that the individual photosensors were not square. A subsequent microscope photograph, shown in Fig. E-1, showed that the photosensor geometry was actually somewhat complex. Contact with the camera manufacturer produced the diagram shown in Fig. E-2, where the photosensor geometry is indeed verified to be complex and therefore not conducive to development of a subpixel centroiding algorithm.

The lesson learned from this preliminary experiment is that focal plane array characteristics will have to be carefully determined and a custom fitted algorithm developed before a subpixel centroiding capability can be realized.

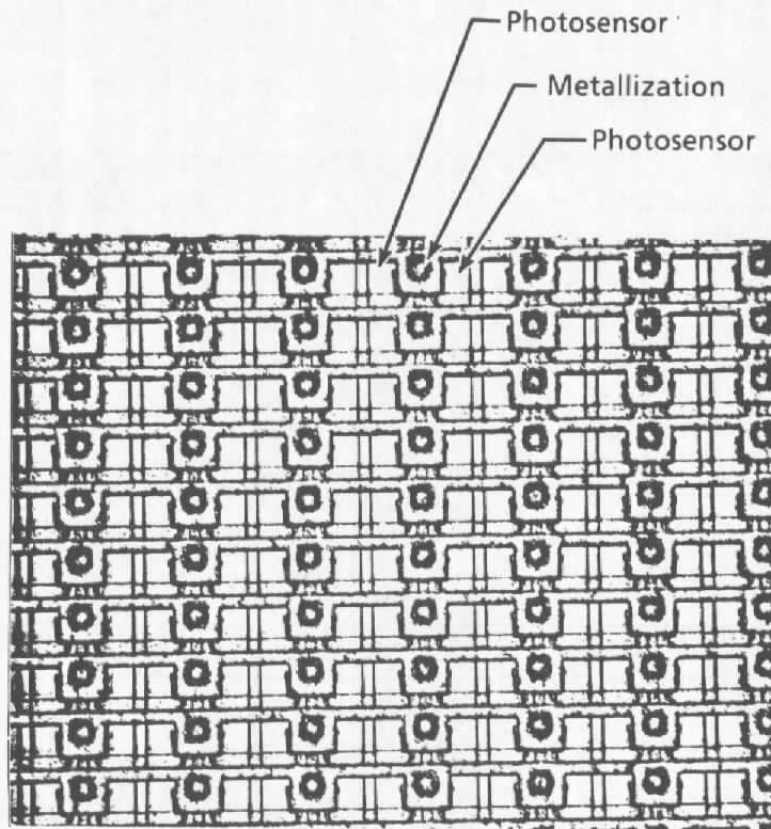


Figure E-1. Microscope photograph of a portion of the MC9256 focal plane array.

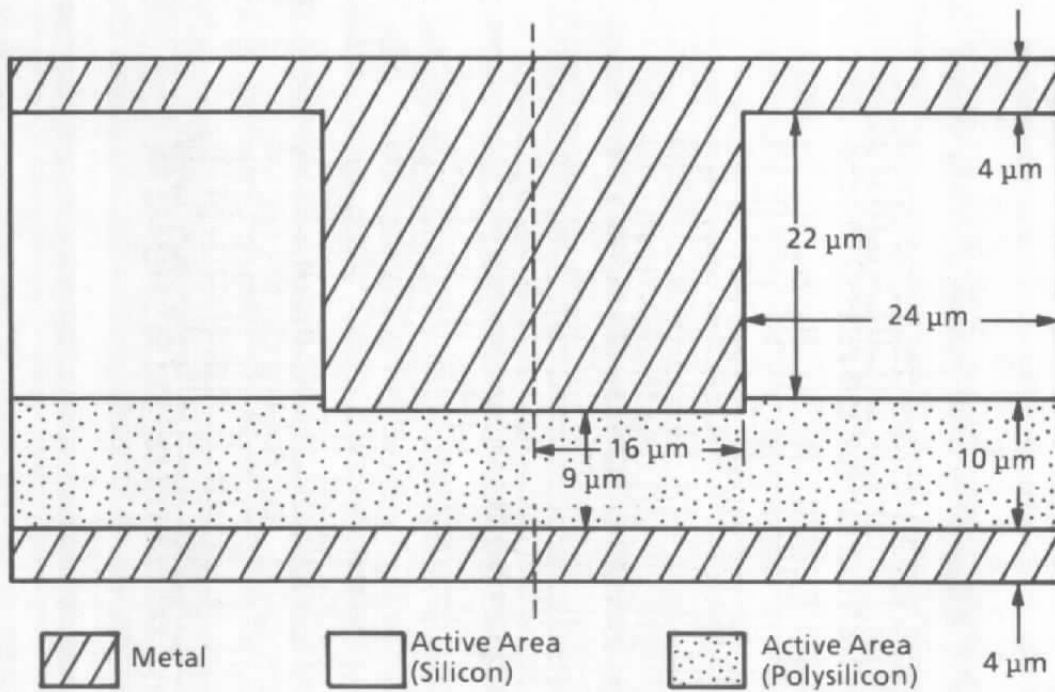


Figure E-2. Manufacturer's diagram for the photosensor geometry in the MC9256 array camera.

APPENDIX F

INTERFEROGRAM ANALYSIS BY FOURIER TRANSFORM INTERFEROMETRY

The primary quantity sought from analysis of interferograms is optical phase after which other quantities can be computed to quantify specific characteristics. For example, optical phase can be used to compute wave front distortions in aberrated light waves, or it may be used to compute changes in index of refraction and subsequently changes in gas density.

The classical approach for determining optical phase involves fringe tracking techniques from which the phase is computed as a shift-from-center measurement for local points along a fringe. Relative to the quantification of the wave front characteristics, the fringe-shift measurements are used to compute point spread functions, modulation transfer functions, encircled energies and Strehl ratios.

This approach has been followed in the aero-optics development program at AEDC. A commercially available software routine called IWAC[®] (Ref. F-1) has heretofore been used to reduce the interferometric measurements, but the results at AEDC showed that uniqueness was not guaranteed, and that the routine failed when the phase variations were high and random. These shortcomings are believed to result from the use of Zernike polynomials and the numerical curve fitting procedures used in IWAC. Further, the results showed that automated fringe tracking failed when the fringe shifts were large, as they typically are in the interferograms of turbulent flows (Ref F-2). Consequently, another approach to determining the optical phase was initiated.

The new method being developed is called Fourier transform interferometry (Ref. F-2). Here, fast Fourier transforms (FFT) and a low-pass digital filter are used to compute the phase directly from digitized measurements of the intensity distribution in the interferograms. No fringe tracking is done, and the resolution of the measurements is limited only by the number of pixels used to sample the interferograms.

Equation (F-1) and Fig. F-1 describe a sinusoidal distribution of intensity along a scan line that is perpendicular to the reference orientation of the fringes,

$$I(x, y) = I_0(x, y) + A [\cos(2\pi F_c x + \phi(x, y))] \quad (F-1)$$

$I(x,y)$ is the measured quantity, and the objective is to isolate $\phi(x, y)$, the optical phase, from $I(x, y)$. The distribution of the reference fringes is given by the angular frequency, $2\pi F_c x$, where F_c is the spatial carrier frequency, and x denotes a specific pixel coordinate in the distribution. The essential requirement needed to isolate $\phi(x,y)$ is F_c which may be

determined from pretest calibration or sometimes directly from the interferogram. Figure F-2 illustrates the power spectrum of $I(x,y)$, and also the shifted spectrum that results from multiplying $I(x,y)$ by $e^{-j2\pi F_c x}$; an FFT is used to compute the spectra. The central band is for $I_0(x,y)$, and the left- and right-side bands are the two components of the modulation term in Eq. (F-1). As illustrated in the shifted spectrum, the right-side band is centered on the origin that allows a low-pass digital filter to be used to isolate it from $I(x,y)$. The filtering is done in the frequency domain, after which an inverse FFT is used to transfer the isolated data back to the space domain. These data are complex numbers, and the optical phase is computed directly as the imaginary term of the complex logarithm, or alternatively as the arc-tangent of the ratio of the imaginary term to the real term.

The major problem is band overlapping that results from either F_c being too small, or from a broadening of the side bands caused by erratic high-frequency spatial variations in the fringes. When F_c is too small, the side bands are indistinct, and the shifted modulation term is inseparable from the other data. Under these conditions, low-pass filtering fails, because part of the $I(x,y)$ spectrum is included and transformed along with the phase information. This event is illustrated in Fig. F-3. Increasing F_c by generating more "wedge-type" reference fringes in the interferogram may make the side bands distinct and thus separable, in which case the phase can be computed as discussed previously. However, if increasing F_c does not make the side bands distinct, the process fails and another technique has to be used, e.g., phase-shift interferometry (Ref. F-3). Theoretical predictions for a "cutoff" F_c that render the demodulation technique faulty are being investigated, but no general results are yet available.

Another problem involves "phase unwrapping." Since $\cos(x + 2\pi) = \cos(x)$, phase angles greater than 2π are embedded in the interval $-\pi \leq x \leq \pi$. Hence, a scheme to "unwrap" phase angles greater than 2π will likely be necessary for the determination of absolute fringe shift measurements of turbulent flow fields; phase unwrapping is unnecessary when only the relative phase is needed to determine additional optical quantities, which is the case for computation of the wave front characteristics. References F-2 and F-4 discuss two different phase-unwrapping algorithms. A phase-unwrapping algorithm is under development at AEDC.

The present capability at AEDC is demonstrated by direct application to interferograms of aero-optics tests. The algorithm is a row-by-row data-reduction routine that requires approximately 6 min to reduce and display an interferogram of 480 by 612 ($r \times c$) pixels. The computations are done quickly (about 45 sec); most of the data-reduction time is used by the image processor to display the phase-computed interferograms corresponding to the true interferograms. Assessment for the present capability is based on qualitative comparisons between the true interferogram and a phase-computed interferogram generated from the calculated phase angles. For an ideal interferogram, $I_0 = A = I_{\max}/2$, and for pixel-gray-

level scale of 0 to 255, $I_0 = A = 127.5$. Thus, the phase-computed interferograms are calculated from

$$I(x,y) = 127.5 \{1 + \cos [2\pi F_c x + \phi(x,y)]\} \quad (F-2)$$

where $\phi(x,y)$ are the computed phase angles in radians.

Figures F-4 and F-5 show some initial results. Each interferogram is made from a single-plate, double-pulse hologram, and the "wedge-type" reference fringes are induced by rotating the holographic reference beam between the laser pulses as described in Section 2.4. Since both laser pulses are recorded on the same plate (note, each laser pulse creates a separate hologram), the relative angle of rotation between the reference beams is fixed. Consequently, the separation angle between the reconstructed object waves is constant, which means the number of "wedge-type" reference fringes, and thus F_c , is fixed. Each interferogram is digitized by a video camera into a 480 by 612 ($r \times c$) pixel array; each pixel is 40 μm square. The spatial carrier frequency, F_c , is computed from analyses of the power spectra of 20 rows ($20 \times$ scans) for each interferogram. For convenience, the interferograms are labeled by the corresponding hologram identification number; also, the true interferogram is shown on the left, and the phase-computed interferogram is shown on the right. Figure F-4 presents results from an FY-87 HEDI test, and those shown in Fig. F-5 are from the FY-88 aero-optics effects test; both tests were conducted in Tunnel C at AEDC.

Relative to Fig. F-4, only Hologram 209 shows good correlation between the original (left) and the phase-computed interferogram. All the others exhibit the effects of the problems discussed previously. Although Holograms 218, 251, 264, and 291 are good overall, the phase-computed interferograms show locations where the fringes break up, appear to branch into Ys, or merge, and Holograms 202, 216, and 274 show basically unusable results. Since increasing F_c is not possible for these interferograms, the phase is unresolved using this technique. Hologram 202 is poor, because the dark splotches on the left prohibited accurate determination of F_c . However, using a smaller aperture on the right side, a good value for F_c was determined, and the corresponding phase-computed interferogram was also good (results not shown). For Holograms 216 and 274, the spatial variations in the fringe shifts are too great and too random, thereby prohibiting determination of an accurate F_c from the too few fringes in each interferogram; the nonsense shown in the corresponding phase-computed interferograms exhibits this point rather well.

Relative to Fig. F-5, all phase-computed interferograms exhibit near congruent identity with the respective true interferograms. The flow-field conditions of the FY-88 aero-optics effects test induced a much lower distortion to the optical waves than did the flow fields of the FY-87 HEDI tests, and therefore, the magnitude of the fringe shifts are much less. Hence, determination of F_c is much better, making determination of the phase much better.

Hologram 9107D20 shows an interesting result, the white upside-down Y fringe. The true interferogram contains this fringe pattern, which indicates the existence of a coherence problem with the ruby laser output, not with the flow field; the Y fringe problem is thought to be caused by poor performance of the pulse ruby laser used to record the holograms. Classical fringe-tracking processes fail at this point; but as shown here, the phase-demodulation process succeeds, because F_c is determined accurately from the true interferogram. Note that the Y region was not used in the determination of F_c ; hence, once F_c is determined accurately, local faults in the interferogram do not have a global effect on the determination of phase.

Additional work on Fourier transform interferometry, plus analyses of the optical phase data are being done at AEDC. Error analyses on F_c are underway; developments for phase unwrapping are programmed; and algorithms for determination of the wave front characteristics of point-spread-function, modulation-transfer-function, encircled energy, and Strehl ratio, all of which are computed from the optical phase, are under development. Additionally, resolutions, sensitivities, and measurement uncertainties will be investigated by making applications to both theoretical and experimental test cases. These results will be presented in another document.

REFERENCES

- F-1. Anderson, D. "Fringe Manual-Version 3. Interferometric Wavefront Analysis Code." Optical Sciences Center, University of Arizona, Tucson, Arizona, April 1982.
- F-2. Takeda, M. et al. "Fourier-Transform Method of Fringe-Pattern Analysis for Computer-Based Topography and Interferometry." *Journal Optical Society of America*, Vol. 72, No. 1, January 1982, pp. 156-160.
- F-3. Stahl, H. P. et al. "Interferometric Phase Measurement Using Pyroelectric Vidicons." *Applied Optics*, Vol. 26, 1987.
- F-4. Huntley, J. M. "Noise-Immune Phase Unwrapping Algorithm." Letters to the Editor, *Applied Optics*, Vol. 28, No. 15, August 15, 1989, pp. 3268-3270.

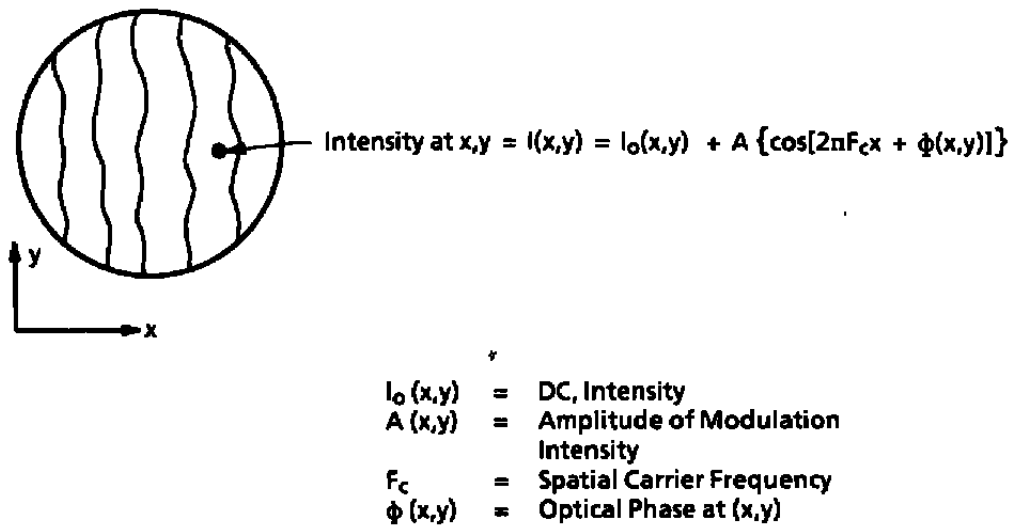


Figure F-1. Illustration of interferogram, intensity map.

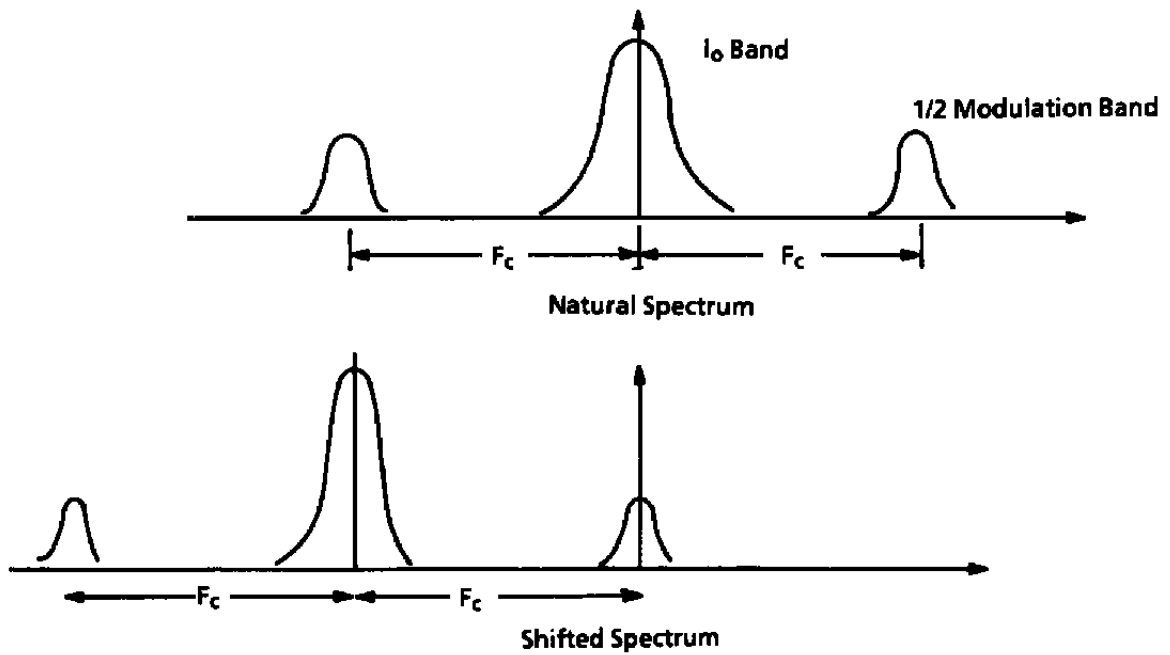


Figure F-2. Illustration of natural and $e^{-2\pi F_c x}$, shifted spectra.

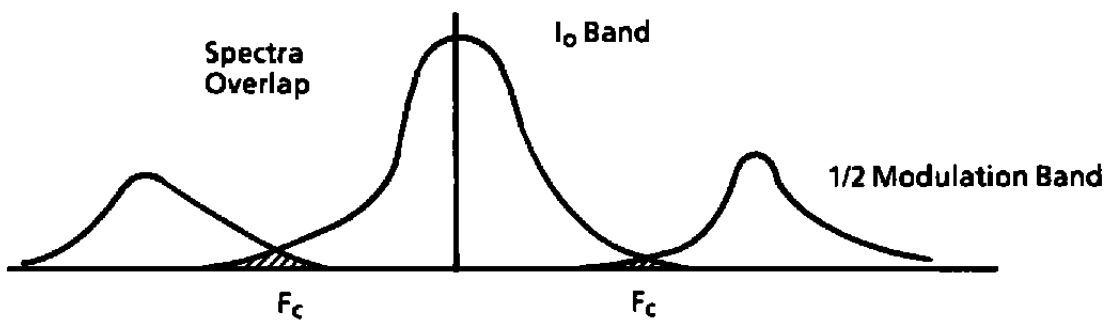
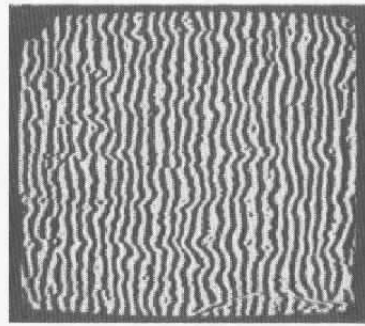
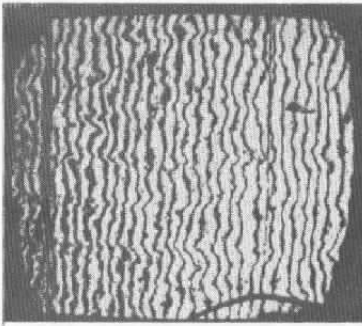
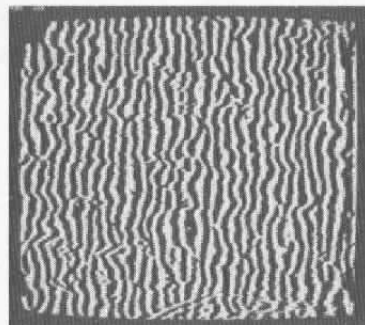
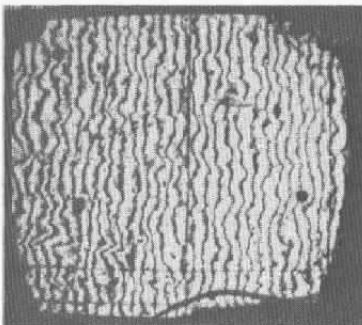


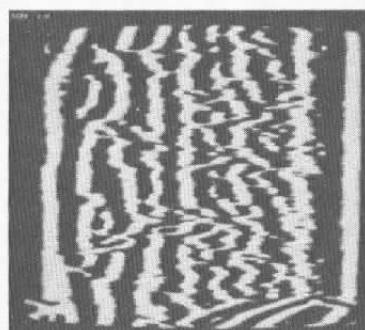
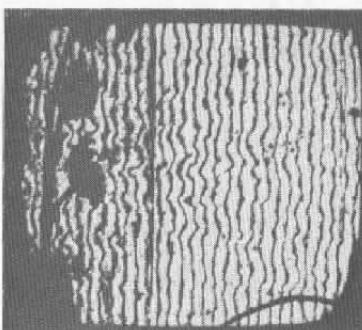
Figure F-3. Illustration of overlapping band caused by small F_c .



a. Hologram 209

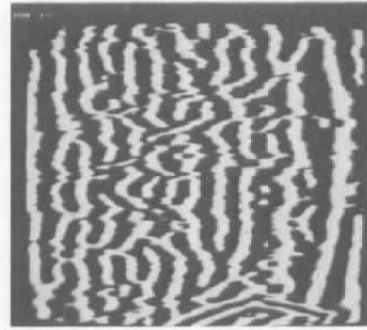
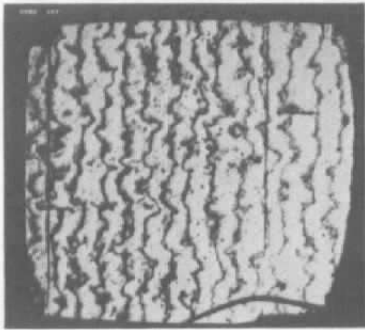


b. Hologram 251

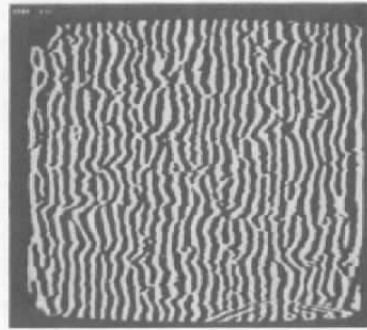
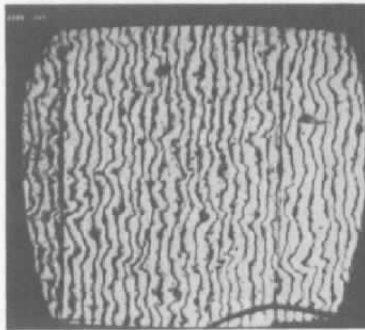


c. Hologram 202

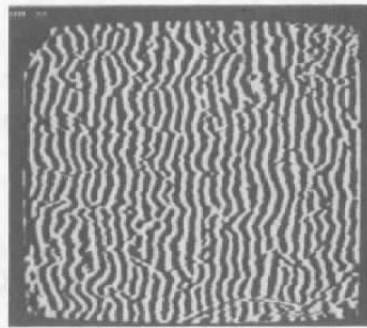
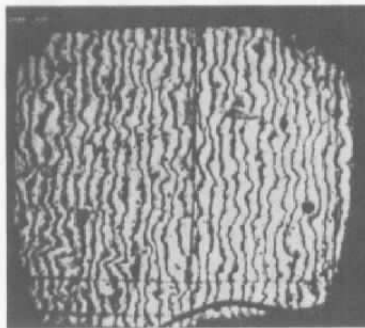
Figure F-4. Holographic and phase-demodulated interferograms.



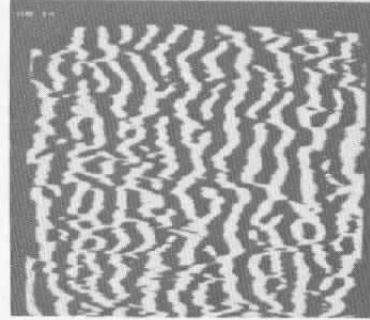
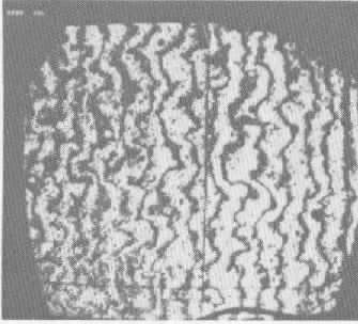
d. Hologram 216



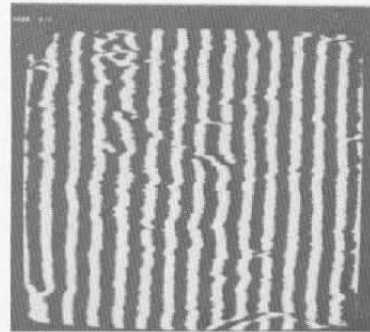
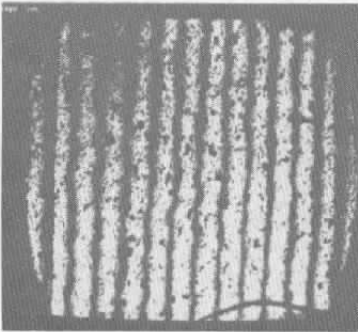
e. Hologram 218



f. Hologram 264
Figure F-4. Continued.

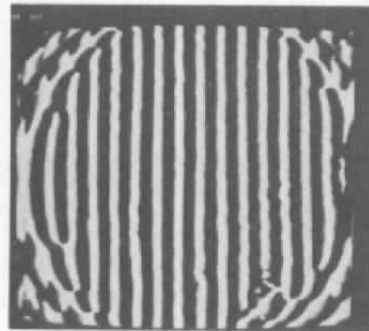
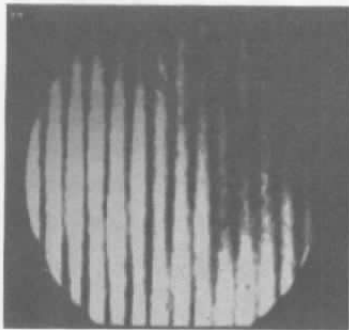


g. Hologram 274

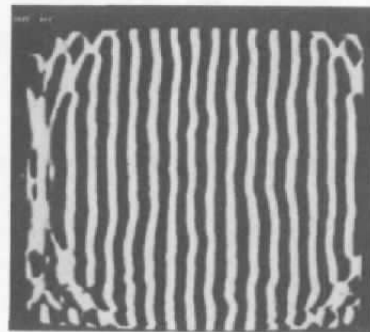
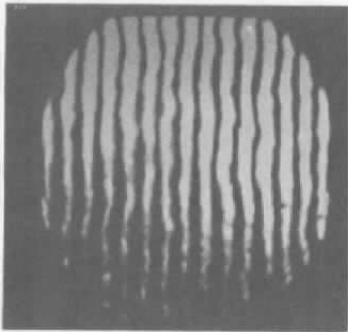


h. Hologram 291

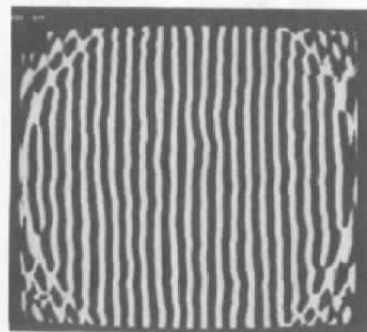
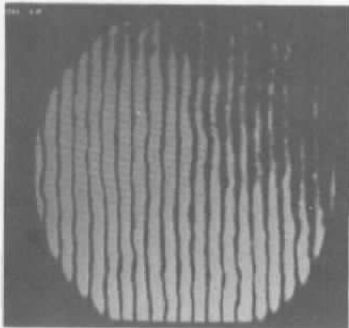
Figure F-4. Concluded.



a. Hologram 4025D60

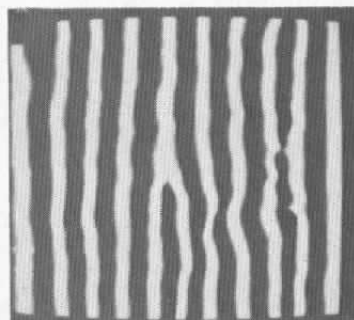
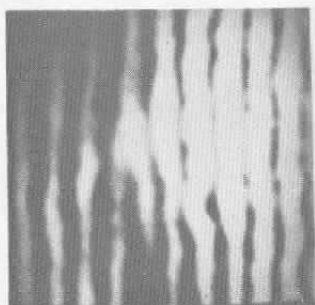


b. Hologram 4327D100

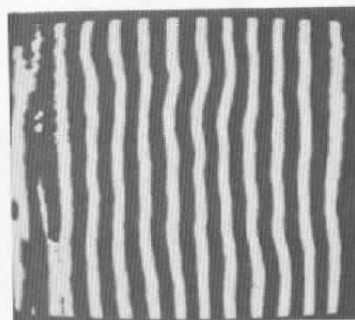
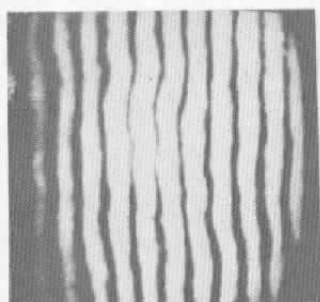


c. Hologram 4318D80

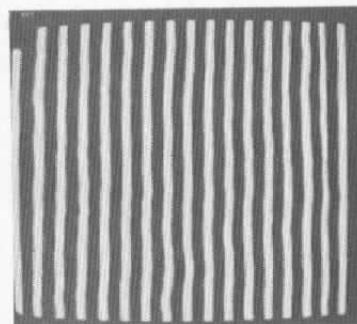
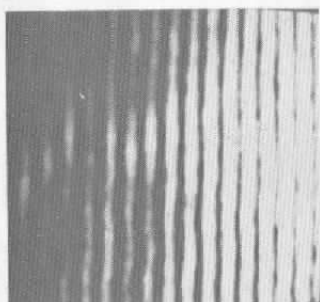
Figure F-5. Holographic and phase-demodulated interferograms.



d. Hologram 9107D20



e. Hologram 4317D80



f. Holograms 4028/4029
Figure F-5. Concluded.

NOMENCLATURE

ECL	Emitter coupled logic
EMI	Electromagnetic interference
F_c	Spatial carrier frequency
f_x	Focal length of optical component x
K	Array camera photosensor spacing (pitch)
M	Angular multiplication factor
m	Lateral image magnification factor
s	Image size, Eq. (1)
TTL	Transistor-transistor logic
v	Acoustic velocity
α	Optical wedge angle
λ	Optical radiation wavelength
$\phi(x,y)$	Phase function